Chronic Hypoxia-Induced Mucus Drives Lung Epithelial PIEZO1 to Promote Pulmonary Fibrosis via ER-Mitochondria Ca^{2+} Transfer

Xupeng Wen[1#], Pan Jiang[2#], Linlin Zheng[3#], Zilong Liu[4#], Yuanjun Yang[1], Yifan Ding[1], Xinxin Du[1], Xiaodan Wu[4], Renhui Huang[5], Shanqun Li[4*], Ming Zhong[1,6*] and Shengyu Hao[1*]

[1]Department of Critical Care Medicine, Zhongshan Hospital, Fudan University, Shanghai, China. [2]Department of Clinical Nutrition, Zhongshan Hospital, Fudan University, Shanghai, China. [3]Department of Gastroenterology and Hepatology, Zhongshan Hospital, Fudan University, Shanghai, China. [4]Department of Pulmonary Medicine, Zhongshan Hospital, Fudan University, Shanghai, China. [5]Department of Thoracic Surgery, Zhongshan Hospital, Fudan University, Shanghai, China. [6]Shanghai Institute of Infectious Disease and Biosecurity, School of Public Health, Fudan University, Shanghai, China

[#] These authors have contributed equally to this work.

[*]Corresponding authors: Shengyu Hao, E-mail: hao.shengyu@zs-hospital.sh.cn; Shanqun Li, E-mail: li.shanqun@zs-hospital.sh.cn; Ming Zhong, E-mail: zhong.ming@zs-hospital.sh.cn.

Conflict-of-interest Statement

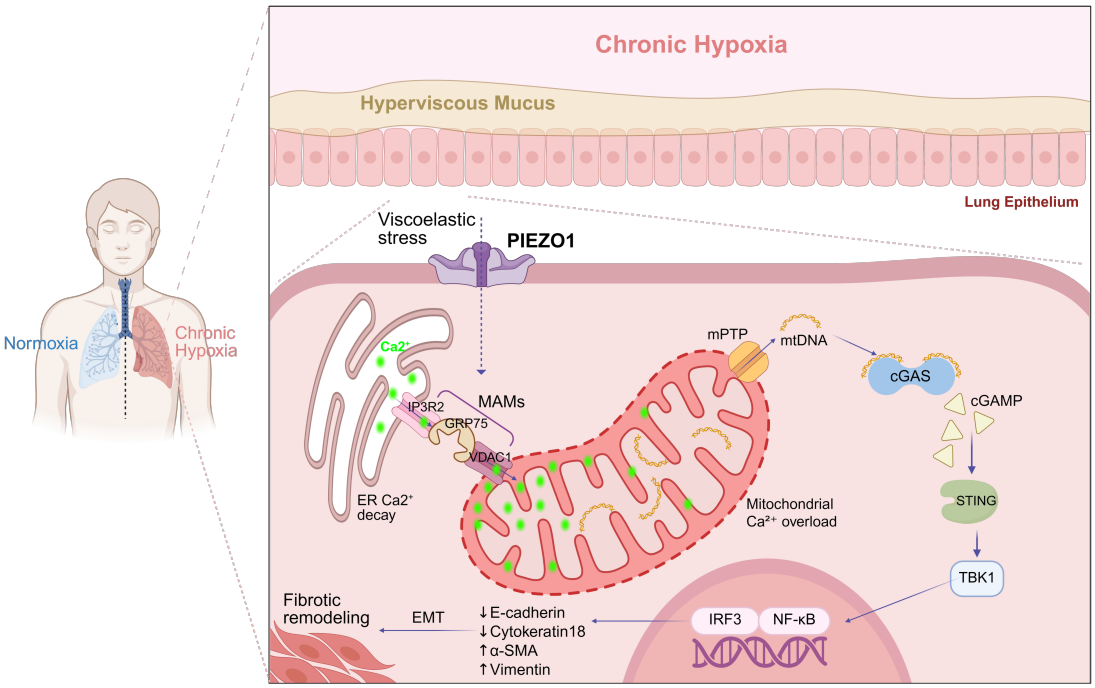
The authors have declared that no conflict of interest exists.

Abstract

Chronic hypoxia (CH) is a hallmark of refractory lung diseases and is closely related to pulmonary fibrotic remodeling, but the underlying mechanisms remain incompletely defined. As the primary barrier, lung epithelial cells are critical sensors of hypoxia. Here, we identify a hypoxia–mucin–PIEZO1 mechanotransduction pathway linking epithelial hypoxic stress to lung structural remodeling. CH increases mucus burden and alters the rheological properties of the epithelial microenvironment, which is associated with enhanced PIEZO1-dependent mechanical responsiveness. Mechanistically, PIEZO1 elicited a composite Ca^{2+} response in which extracellular entry remained detectable, while IP3R-associated ER-store mobilization served as a prominent intracellular amplification step feeding IP3R2–GRP75–VDAC1-dependent ER-to-mitochondrial Ca^{2+} transfer. This promoted mitochondrial Ca^{2+} overload, mPTP opening, mtDNA release, epithelial cGAS–STING activation, and EMT-associated remodeling. Crucially, lung epithelial PIEZO1 deletion or pharmacological inhibition of this axis, including treatment with the mucolytic agent N-acetylcysteine or cGAS-STING inhibitors, reduces CH-induced EMT and fibrotic remodeling. Our findings identify a mucus-associated mechanotransduction pathway that contributes to CH-associated pulmonary fibrotic remodeling and highlight potential intervention points within the mucus–PIEZO1 signaling axis.

Keywords: PIEZO1, chronic hypoxia, mucus, pulmonary remodeling, epithelial-mesenchymal transition

Graphical abstract



Introduction

Pulmonary fibrosis is a devastating end-stage manifestation of multiple chronic respiratory diseases, characterized by excessive extracellular-matrix deposition, parenchymal scarring, and progressive structural remodeling [1]. Chronic hypoxia (CH) constitutes a cardinal pathophysiological hallmark across a spectrum of major pulmonary disorders [2], including chronic obstructive pulmonary disease (COPD) [3], severe asthma [4], obstructive sleep apnea-hypopnea syndrome (OSAHS) [5], and high-altitude exposure-related lung disease [6], and is inextricably linked to progressive structural remodeling. Traditionally, chronic hypoxia (CH) has been regarded as a secondary consequence of structural destruction of the lung. However, accumulating evidence suggests that CH may actively contribute to epithelial dysfunction and pulmonary remodeling [2, 7]. Uniquely, the lung epithelium lining pulmonary surfaces derives oxygen primarily from luminal inspired air rather than the submucosal vasculature, positioning it as a frontline sensor of hypoxic stress. Epithelial-mesenchymal transition (EMT) acts as a fundamental driver of pulmonary fibrotic remodeling, characterized by the loss of epithelial markers and the acquisition of mesenchymal features [8]. Hypoxia profoundly alters epithelial homeostasis and promotes pathological scarring through EMT [9]. Although hypoxia-inducible factor (HIF)–mediated transcriptional regulation accounts for part of the metabolic adaptation

to hypoxia, it does not fully explain how CH, as a biochemical signal, is converted into the altered mechanical microenvironment accompanying chronic lung remodeling. These observations suggest the existence of an as yet insufficiently characterized "chemical-to-mechanical" signal transduction axis linking CH to the development of pulmonary fibrotic remodeling.

PIEZO1 is a mechanically activated cation channel that senses membrane tension and diverse mechanical properties of the extracellular environment. Recent studies have implicated PIEZO1 in pulmonary myofibroblast activation, mechanically aggravated lung injury, and immune-cell mechanotransduction, while its identity as a mechanically activated cation channel is well established [10-13]. However, PIEZO1 activation is strictly force-dependent, creating a paradox within the biochemical context of CH, which inherently lacks overt external physical stretch. Identifying the endogenous "invisible physical trigger" that sustains lung epithelial PIEZO1 activation under CH remains a critical knowledge gap in understanding fibrotic remodeling.

Mucus remodeling represents a plausible link between hypoxic signaling and epithelial mechanotransduction. Chronic airway epithelial hypoxia increases the production of the gel-forming mucins MUC5AC and MUC5B and enhances epithelial fluid absorption, resulting in mucus hyperconcentration [2]. Increasing mucus concentration raises its osmotic and viscoelastic moduli and impairs mucus transport [3, 14]. We

hypothesize that the CH-induced formation of a high-viscosity, low-mobility mucus microenvironment imposes a sustained physical load on the underlying lung epithelial cells. This aberrant viscoelastic stress exerted by the mucus likely serves as the elusive endogenous mechanical source that enhances PIEZO1-dependent mechanical responsiveness in hypoxic environments. This concept aligns with recent findings by Oliva et al. demonstrating that PIEZO1 regulates the mechanotransduction of matrix viscoelasticity [15]. However, whether lung epithelial cells sense this CH-secondary mechanical stress via PIEZO1 and transduce it into pro-fibrotic signaling remains to be elucidated.

In this study, we propose a "mucus-mechanotransduction" framework linking CH-induced remodeling of the epithelial secretory environment to pulmonary fibrotic remodeling. We demonstrate that CH increases gel-forming mucin production and alters the rheological properties of the epithelial microenvironment, thereby enhancing PIEZO1 expression and PIEZO1-dependent mechanical responsiveness. Rather than excluding its canonical role in mechanically activated cation entry [13, 16, 17], our findings indicate that PIEZO1 elicits a composite Ca^{2+} response in which IP3R-associated ER-store mobilization serves as a prominent intracellular amplification step. This response is coupled to ER-to-mitochondrial Ca^{2+} transfer through the IP3R2–GRP75–VDAC1 machinery at mitochondria-associated membranes (MAMs) [18, 19], leading to mitochondrial Ca^{2+} overload, mPTP opening, mtDNA release, and epithelial

cGAS–STING activation. These events are associated with EMT-related epithelial remodeling and fibroblast-activating paracrine signaling. Collectively, our study elucidates the molecular mechanism by which lung epithelial PIEZO1 integrates upstream mucus-derived mechanical cues with downstream signaling cascades to contribute to CH-associated pulmonary fibrotic remodeling. Complementary mucin-loading, genetic, and pharmacological approaches further support the contribution of this pathway to CH-associated pulmonary fibrotic remodeling. These findings provide a mechanobiological perspective on the pathogenesis of pulmonary fibrosis and provide a rationale for potential interventions targeting CH-induced progressive structural pulmonary remodeling.

Materials and Methods

The key resources used are listed in Table S2.

More detailed methods can be found in the supplementary materials.

Human samples: Human lung tissue samples (tumor-adjacent non-neoplastic tissues) were collected from patients with COPD (n = 10) and non-COPD control donors (n = 6) undergoing thoracic surgery for lung cancer at Zhongshan Hospital, Fudan University. Detailed demographic and clinical characteristics are summarized in Table S1. We used COPD-associated samples primarily because chronic hypoxemia/hypoxic stress is a well-recognized feature of advanced COPD, allowing us to ask whether a

hypoxia-associated epithelial program might overlap with the pathway defined in our models.

Study approval: The collection and use of human tissues were approved by the Institutional Review Board of Zhongshan Hospital, Fudan University (Approval No. B2025-657; ClinicalTrials.gov Identifier: NCT07236541), in compliance with the Declaration of Helsinki. Written informed consent was obtained from all participants. Furthermore, all animal experiments were approved by the Institutional Animal Care and Use Committee (IACUC) of Zhongshan Hospital, Fudan University (Approval No. 2024-087), and performed in accordance with the NIH Guide for the Care and Use of Laboratory Animals and the ARRIVE guidelines.

Generation of epithelial Piezo1 CKO mice: Procedures for lung epithelial cell-specific *Piezo1* conditional knockout (CKO, *Piezo1*$^{flox/flox;}$ *Sftpc-Cre*^{ERT2}) mice have been previously described [11]. Briefly, *Piezo1*$^{flox/flox}$ mice (Cyagen Biosciences) were crossed with *Sftpc-Cre*^{ERT2} mice (GemPharmatech). Age- and weight-matched *Piezo1*$^{flox/flox}$ littermates were used as controls. To induce Cre recombination, mice (3-4 weeks old) received intraperitoneal (i.p.) injections of tamoxifen (75 mg/kg) once daily for 5 consecutive days. All experiments were commenced 1 week after the final tamoxifen injection. Genotyping was confirmed by PCR using primers listed in Table S4. All mice were on a C57BL/6J background. The wild-type C57BL/6J mice involved

in this study were all purchased from Cyagen Biosciences. The mice used in the study were 6- to 8-week-old females or males (no sex difference was observed). The mice were housed under specific pathogen–free conditions at approximately 22°C with humidity set at 40%–70% and a 12-hour light/12-hour dark cycle.

Chronic hypoxia exposure in mice: Mice were randomly assigned to normoxia (Nor) or chronic hypoxia (CH) groups. CH mice were housed in a normobaric chamber maintained at 9% O_2 via continuous N_2 flushing for 5 weeks. Soda lime and silica gel were utilized within the chamber to absorb CO_2 and control humidity, respectively. Chambers were opened twice weekly for <30 min for standard husbandry. Nor control mice were maintained in ambient room air ($\approx$21% O_2) under otherwise identical conditions.

AAV6-mediated pulmonary Piezo1 knockdown in mice: To achieve localized knockdown of *Piezo1* in the lung epithelium, Adeno-associated virus serotype 6 (AAV6) vectors expressing short hairpin RNA (shRNA) targeting *Piezo1* (AAV6-sh*Piezo1*) or a non-targeting scrambled control (AAV6-shScramble) driven by the U6 promoter were administered via intratracheal instillation, as previously described [20]. Mice were maintained for 21 days post-instillation to allow for optimal viral transduction and gene silencing prior to chronic hypoxia exposure. Target sequences for shRNAs are listed in Table S5.

Pharmacological inhibition studies in mice: CH-exposed mice received intratracheal (i.t.) instillation of the mucolytic agent N-acetylcysteine (NAC; 50 mg/mL, pH: 7.4, 40 μL/mouse) every three days. For pharmacological pathway interrogation, Yoda1 was administered intraperitoneally at 0.2 mg/kg, and the STING inhibitor H-151 was administered intraperitoneally at 10 mg/kg every 3 days during CH exposure. Vehicle-treated groups received matched solvent according to the same schedule.

Preparation and intratracheal administration of mucin-coated beads: Mucin-coated beads were prepared by covalently coupling porcine gastric mucin M2378 (Sigma-Aldrich) to 2-μm NHS-activated magnetic beads (BeaverBio, Cat. 70703-1). Following coupling, residual NHS groups were quenched with glycine, and unbound mucin was removed by repeated washing. Bare beads underwent the same procedure without mucin. Beads were resuspended at 10 mg/mL in sterile PBS, and mice received 50 μL of bare or mucin-coated bead suspension intratracheally on days 0 and 7; lungs were harvested on day 14. Groups included bare beads, mucin-coated beads, mucin-coated beads plus NAC, and mucin-coated beads administered to epithelial *Piezo1* CKO mice. Bead-associated mucin loading was quantified and normalized to bead mass. This model was designed as a hypoxia-independent sufficiency test of exogenous mucin-associated airway burden, not a reconstruction of native airway mucus. Potential differences in composition, glycosylation, polymer organization, and rheological

194 behavior, together with bead immobilization, limit extrapolation to endogenous
195 MUC5AC/MUC5B-containing mucus.
196
197 *Cell culture*: Human lung epithelial BEAS-2B cells (ATCC) were cultured in BEGM
198 supplemented with the SingleQuot kit (Lonza) at 37°C with 5% CO_2 atmosphere. Cell
199 identity was authenticated via short tandem repeat (STR) profiling, and cultures were
200 routinely screened for mycoplasma contamination. To maintain phenotypic stability,
201 all experiments were performed using cells between passages 3 and 10. Commercial
202 primary human bronchial epithelial cells (HBECs; ATCC PCS-300-010) were cultured
203 in Airway Epithelial Cell Basal Medium (ATCC PCS-300-030) supplemented with
204 Bronchial/Tracheal Epithelial Cell Growth Kit (ATCC PCS-300-040) at 37°C with 5%
205 CO_2. Cells were maintained as submerged monolayers, used at passages P1–P2, and
206 subcultured at 70–80% confluence. MRC-5 human lung fibroblasts (ATCC CCL-171)
207 were cultured in EMEM containing 10% FBS and were used before passage 30. All
208 cultures were routinely tested for mycoplasma contamination.
209
210 *In vitro chronic hypoxia model*: To mimic the chronic hypoxic microenvironment,
211 BEAS-2B or primary HBECs were cultured in a tri-gas incubator (Thermo Fisher
212 Scientific) strictly maintained at 1% O_2, 5% CO_2, and 94% N_2 at 37°C for 72 hours.
213 Crucially, to prevent oxygen fluctuations, the culture medium was not changed during
214 this exposure period. Parallel normoxic control cells were maintained under standard

conditions (21% O_2, 5% CO_2) at 37°C. For moderate-hypoxia validation, cells were exposed to 5% O_2 for 72 h.

Conditioned-medium transfer and rheological modulation: To assess the effects of the hypoxia-conditioned extracellular environment without direct hypoxic exposure, a conditioned-medium (CM) transfer model was established. Donor BEAS-2B cells (3×10^5 cells/well) grown to 70–80% confluence were washed twice with PBS to remove residual metabolites, replenished with fresh BEGM, and cultured under normoxia (21% O_2, 5% CO_2) or chronic hypoxia (1% O_2, 5% CO_2) for 72 hours. Supernatants were centrifuged (1,000 × g, 10 min, 4°C) to obtain Nor-CM and CH-CM. The media were not subjected to 0.22-μm filtration to minimize potential loss or alteration of mucin-associated assemblies; non-mucin macromolecules and extracellular particles could therefore remain. Naïve recipient BEAS-2B cells (60–70% confluence) were incubated with Nor-CM or CH-CM under normoxic conditions for 24 hours. To perturb mucin-associated rheology, CH-CM was co-treated with the mucolytic agent N-acetylcysteine (NAC; 10 mM, pH 7.4) to reduce mucin disulfide bonds, using PBS as a vehicle control. For complementary viscosity modulation, an inert viscosifier, methylcellulose (MC, 0.6–0.8% w/v), was dissolved in medium (stirred 12–16 h at 4°C). The MC concentration was adjusted batch-wise to match the apparent viscosity of CH-CM at a shear rate of 1 s^{-1}, as determined by rotational rheometry. Following the 24-hour treatment, cells were harvested for PIEZO1 and EMT marker analysis.

CRISPR/Cas9-mediated gene knockout and siRNA silencing: The *PIEZO1*-knockout BEAS-2B cell line (*PIEZO1*-KO) was generated using the CRISPR/Cas9 genome editing system (Genomeditech). Two sgRNAs targeting distinct regions of the human *PIEZO1* gene were cloned into the PGMLV-SpCas9 vector (target sequences are listed in Table S6). For transient gene silencing, cells at 60% confluency were transfected with 100 nM *GRP75* and *HIF1α* siRNA or a non-targeting control (NC) siRNA using the riboFECT CP Transfection Kit (RiboBio) according to the manufacturer's protocol (siRNA sequences are listed in Table S7). The efficiencies of both *PIEZO1* knockout, *GRP75* and *HIF1α* knockdown were validated by Western blotting 48 h post-transfection.

Rheological characterization: Independent batches of Nor-CM, CH-CM, and NAC-treated CH-CM were analyzed using cone-and-plate rotational rheometry [14, 21]. A strain sweep was first performed to identify the linear viscoelastic range, followed by a frequency sweep to determine the storage modulus (G′) and loss modulus (G″). G′ and G″ at 1 Hz were used for group comparisons. Apparent viscosity was measured under controlled shear, and the value at 1 s^{-1} was reported. Each biological replicate represented an independently prepared conditioned-medium batch.

Cell-attached pressure-clamp electrophysiology: Mechanically activated currents were recorded in the cell-attached configuration after 24 h conditioning with Nor-CM, CH-CM, NAC-treated CH-CM, methylcellulose-containing medium, or CH-CM + GsMTx4. Before recording, all cells were transferred to the same standardized recording solution to preserve seal stability. Negative-pressure steps from 0 to −60 mmHg were applied through the recording pipette in 10-mmHg increments. Pressure–current relationships, peak currents at −40, −50, and −60 mmHg, activation thresholds, responsive-cell proportions, and current-inactivation kinetics were analyzed. Recordings were obtained from three independent cell preparations. The protocol was adapted from established PIEZO1 pressure-clamp methods [13].

Histological analysis and scoring: To preserve alveolar architecture, mouse lungs were inflation-fixed with 4% paraformaldehyde via intratracheal instillation. Following 24-hour fixation and paraffin embedding, tissue sections were stained with hematoxylin and eosin (H&E) to evaluate lung injury using Smith's scoring system (0–4 points evaluating edema, atelectasis, hyaline membrane formation, inflammation, and hemorrhage). Fibrotic remodeling was quantified on Masson's trichrome-stained sections using the Ashcroft scale.

Single-cell RNA-seq processing and analysis: Publicly available scRNA-seq datasets, including human datasets GSE158942, GSE227508, GSE135893, GSE136831, and

GSE190889 and the rat dataset GSE273062, were processed using Seurat (v4.0) in R (v4.2). To prevent cross-species integration artifacts, human and rodent datasets were analyzed independently. Cells expressing <200 genes or >5% mitochondrial transcripts were excluded. Data were log-normalized, and the top 2,000 highly variable genes were selected for PCA. Sample-specific batch effects were corrected using Harmony. Dimensionality reduction and clustering were performed using UMAP (top 20 Harmony embeddings) and the Louvain algorithm (resolution 0.6). Cell types were annotated based on canonical markers ($log_2FC > 0.25$, minimum expression > 25%). Cell types were annotated according to canonical lineage markers, and epithelial populations were further subclustered into AT I, AT II, basal, secretory, goblet, and ciliated cells where these lineages were represented in the corresponding dataset. Crucially, to mitigate single-cell amplification noise and account for biological replicates, differential expression of human *PIEZO1* and rat *Piezo1* was evaluated using a pseudo-bulk aggregation strategy. Functional enrichment (GSEA) was performed using the clusterProfiler package.

Measurements of intracellular Ca^{2+}: Changes in intracellular Ca^{2+} concentration were monitored using the fluorescent indicator Fluo-4 AM. BEAS-2B cells seeded in 96-well black plates or 35-mm confocal dishes were washed with Ca^{2+}-free HBSS and incubated with 5 μM Fluo-4 AM and 0.02% Pluronic F-127 for 30 min at 37°C in the dark. Following washing, cells were rested in fresh HBSS for 20 min at room

298 temperature to allow complete esterase hydrolysis. Fluorescence kinetics
299 (excitation/emission at 494/516 nm) were recorded using a microplate reader
300 (Molecular Devices, Sunnyvale, CA, USA). Baseline fluorescence (F_0) was established
301 for 50 s, followed by the automated injection of 2× concentrated stimuli (e.g., CH-CM,
302 20 μM Yoda1). Fluorescence was continuously recorded for 300 s, and data are
303 expressed as the relative fluorescence change: $\Delta F / F_0 = (F_t - F_0) / F_0$. For mechanistic
304 inhibition, cells were pre-incubated with GsMTx4 (5 μM), Xestospongin-C (10 μM),
305 or NAC (10 mM) for 30 min prior to detection. To dissect Ca^{2+} sources, extracellular
306 Ca^{2+} was chelated by injecting 5 mM EGTA and cells were stimulated in nominally
307 Ca^{2+}-free buffer, followed by re-addition of $CaCl_2$ to a final concentration of 2 mM to
308 assess extracellular Ca^{2+} entry. Spatial Ca^{2+} distribution was visualized using a confocal
309 laser scanning microscope (Leica, 488 nm excitation).
310
311 *Measurements of ER Ca^{2+}*: To precisely dissect endoplasmic reticulum (ER) Ca^{2+}
312 dynamics and steady-state stores, a genetically encoded ER Ca^{2+} sensor (G-CEPIA1er)
313 and a low-affinity fluorescent dye (Mag-Fluo-4 AM) were employed. Mag-Fluo-4 AM
314 was used only as a complementary low-affinity organellar Ca^{2+}-sensitive readout
315 because its fluorescence is not exclusively determined by ER Ca^{2+}. For real-time ER
316 Ca^{2+} release kinetics, BEAS-2B cells (1×10^6) were electroporated with 2 μg of G-
317 CEPIA1er plasmid (Addgene, #58215) using the Cell Line Nucleofector Solution V
318 (Lonza). Post-transfection (24–48 h), correct subcellular ER localization was verified

by co-staining with 1 μM ER-Tracker Red for 30 min at 37°C via confocal microscopy (63×, Leica). ER Ca^{2+} efflux, which manifests as a rapid fluorescence decrease, was monitored using a microplate reader. Following a 50-s baseline (F_0), stimuli (e.g., CH-CM) were automatically injected. To quantify release efficiency, the ER Ca^{2+} decay rate constant (K [s^{-1}]) was calculated using a single-exponential decay fit. IP3R-dependence was confirmed by pre-incubating cells with Xestospongin-C (10 μM) for 30 min prior to stimulation. To deplete endoplasmic reticulum Ca^{2+} stores, cells were pretreated with thapsigargin (1 μM) for 10 min in Ca^{2+}-free buffer before stimulation. Following stringent washing to minimize cytosolic background, cells were harvested and analyzed via flow cytometry (BD FACSAria). The mean fluorescence intensity (MFI) in the FITC channel was recorded to reflect ER-enriched Ca^{2+}-sensitive signal.

Measurements of mitochondrial Ca^{2+}: Cells were loaded with the mitochondria-enriched Ca^{2+} indicator Rhod-2 AM (Yeasen) supplemented with 0.02% Pluronic F-127. After incubation for 30 minutes at 37°C, cells were washed and counterstained with MitoTracker Green for an additional 30 minutes to visualize mitochondrial morphology. Fluorescence images were acquired using a confocal laser scanning microscope (63×, Leica). The co-localization of Ca^{2+} with mitochondria was analyzed to quantify relative mitochondrial Ca^{2+} levels.

Visualization of ER-Mitochondria Interactions: Cells were first incubated with ER-Tracker Green (1 μM, Beyotime) for 20 minutes, followed by counterstaining with MitoTracker Red (200 nM, Beyotime) for 30 minutes at 37°C. After washing with PBS, fluorescence images were acquired using a laser scanning confocal microscope (63×, Leica). The extent of ER-mitochondria interaction was evaluated by analyzing the spatial co-localization of the ER and mitochondria fluorescence signals via ImageJ software.

Transmission Electron Microscopy (TEM): To visualize ultrastructural changes and mitochondria-associated ER membranes (MAMs), BEAS-2B cells were harvested, fixed, and processed following the protocol described previously [22]. Images were acquired using a JEOL JEM-1400Flash electron microscope (Japan).

AB-PAS staining: Paraffin-embedded lung sections or 4% PFA-fixed cells were subjected to Alcian Blue/Periodic Acid-Schiff staining to visualize acidic and neutral mucosubstances, respectively. Total mucin accumulation was quantified as the AB-PAS-positive area normalized to the epithelial perimeter or total epithelial ROI. For subtype analysis, the original RGB images were subjected to color separation in ImageJ/Fiji using identical analysis parameters within each staining batch. Alcian blue-dominant and PAS-dominant signals were quantified separately and expressed as positive area relative to the analyzed epithelial ROI. Where both signals were detected

within the same region, the area was classified as mixed staining. Multiple non-overlapping fields were first averaged within each biological sample before statistical analysis.

Statistical Analysis: Data from at least three independent biological replicates are presented as mean ± SD. Analyses were performed using GraphPad Prism 9.0. Normality and homogeneity of variance were assessed before parametric testing. Two-group comparisons were evaluated using two-tailed paired or unpaired Student's t-tests. Multiple comparisons were analyzed via one- or two-way ANOVA followed by Tukey's post hoc test. Non-parametric alternatives were employed when parametric assumptions were violated. Statistical significance was defined as $P < 0.05$ (* $P < 0.05$, ** $P < 0.01$, *** $P < 0.001$, **** $P < 0.0001$, ns: not significant).

Results

CH induces pulmonary fibrotic remodeling with EMT-associated changes

To characterize CH-associated pulmonary remodeling in vivo, mice were exposed to 9% O_2 for 5 weeks (Fig. 1A). H&E staining revealed alveolar septal thickening and inflammatory cell accumulation, accompanied by an increased Smith lung injury score in CH-exposed mice compared with normoxic controls (Fig. 1B). Masson's trichrome staining demonstrated marked peribronchial and interstitial collagen deposition, with a corresponding increase in the Ashcroft score (Fig. 1C). Consistent with these histological changes, lung hydroxyproline content was significantly increased after CH

exposure (Fig. 1D). Lung concentrations of IL-6, TGF-β, and IL-13 were also elevated in the CH group (Fig. 1E–G), indicating concurrent inflammatory and profibrotic signaling.

Bulk RNA-seq analysis further identified enrichment of Gene Ontology terms related to extracellular matrix organization, collagen-containing extracellular matrix, epithelial-to-mesenchymal transition, response to hypoxia, inflammatory responses, and calcium-related signaling (Fig. 1H). WikiPathways analysis independently identified lung fibrosis among the enriched pathways in CH lungs (Fig. S1A). In addition, GSEA of published epithelial transcriptomic datasets representing COPD-associated and hypoxia-exposed contexts showed significant enrichment of an EMT-associated gene signature (Fig. 1I).

Consistent with these transcriptomic profiles, qPCR and Western blot (WB) analyses of lung tissues showed significant upregulation of mesenchymal markers (α-SMA/*Acta2*, Vimentin/*Vim*) with a concomitant loss of epithelial markers (E-cadherin/*Cdh1*, Cytokeratin-18/*Krt18*) (Fig. 1J, K). Immunofluorescence (IF) staining further supported these EMT-associated changes in the lung epithelium (Fig. 1L, M). Furthermore, immunohistochemistry (IHC) revealed a marked accumulation of α-SMA that prominently localized to the hyperplastic epithelial regions within fibrotic lesions following CH exposure (Fig. 1N). Collectively, these data indicate that CH induces

pulmonary fibrotic remodeling accompanied by activation of an epithelial EMT-associated program.

Because the subsequent mechanistic experiments used 1% O_2 exposure for 72 h, we next assessed whether this regimen caused overt cytotoxicity and whether epithelial barrier alterations preceded the later EMT-associated phenotype. Cellular metabolic activity was preserved at 24 h but showed modest, oxygen-dependent reductions at 48 and 72 h, with the greatest decrease observed under 1% O_2 (Fig. S1B). In contrast, LDH release remained unchanged at both 24 and 72 h across the 21%, 5%, and 1% O_2 conditions (Fig. S1C), arguing against extensive lytic cell death. At 24 h, TEER was reduced in an oxygen-dependent manner (Fig. S1D), accompanied by decreased expression of the junctional genes CDH1 and TJP1 (Fig. S1E, F). By contrast, FN1 showed only a modest increase under 1% O_2, whereas ACTA2 remained unchanged (Fig. S1G, H). These results indicate that early epithelial barrier dysfunction precedes the robust EMT-associated program observed after prolonged hypoxia and is not accompanied by substantial membrane injury.

CH upregulates the expression of PIEZO1 in lung epithelial cells

Given the contribution of mechanotransduction to pulmonary remodeling, we first screened a panel of mechanosensitive ion channels in BEAS-2B cells exposed to 1% O_2 for 72 h. Among the candidates examined, PIEZO1 exhibited the highest basal

expression and the most pronounced hypoxia-induced increase (Fig. 2A). Re-analysis of three independent datasets further showed increased PIEZO1 expression in primary airway basal cells from patients with COPD versus control donors (GSE158942), hypoxia-exposed human bronchial epithelial cells (GSE227508), and hypoxia-exposed rat lungs (GSE273062) (Fig. 2B). Cell-type-resolved analysis of the multi-lineage hypoxia dataset identified AT I, AT II, basal, secretory, goblet, and ciliated epithelial populations and showed a consistent increase in PIEZO1 expression across these major epithelial subsets (Fig. 2C; Fig. S2A–C).

To directly assess relevance to human fibrotic lung disease, we additionally analyzed three independent human pulmonary fibrosis/IPF scRNA-seq datasets (GSE135893, GSE136831, and GSE190889). PIEZO1 expression was increased in AT I, AT II, basal, secretory, goblet, and ciliated epithelial populations in fibrotic/IPF lungs, whereas no significant difference was detected in the residual “other” epithelial population (Fig. S2D–G). These findings extend the hypoxia-associated observation to established human fibrotic lung disease.

We next validated PIEZO1 expression experimentally. In mouse lungs, CH increased Piezo1-positive staining and whole-lung Piezo1 protein abundance (Fig. 2D, E). Double immunofluorescence further demonstrated increased Piezo1 signal within SPC-positive AT2 cells after CH exposure (Fig. 2F). In BEAS-2B cells, prolonged hypoxia

induced a time-dependent increase in PIEZO1 protein expression, accompanied by increased α-SMA, and the increase in cellular PIEZO1 fluorescence was independently confirmed by immunofluorescence (Fig. 2G; Fig. S2H).

To assess clinical relevance, we analyzed lung tissue samples from patients with COPD (n=10) and non-COPD control donors (n=6) (Table S1). PIEZO1 protein abundance and PIEZO1-positive tissue area were increased in COPD samples compared with donor controls, together with structural remodeling and collagen accumulation (Fig. 2H–K). Cell-type-resolved double immunofluorescence showed that this increase was most pronounced within KRT18-positive epithelial regions. A smaller increase was detected within CD31-positive endothelial regions, whereas no significant disease-associated enrichment was observed within CD68-positive macrophage or α-SMA-positive contractile compartments (Fig. 2L). Collectively, these data support epithelial-predominant PIEZO1 upregulation across experimental hypoxia and human chronic lung disease contexts.

Epithelial PIEZO1 deficiency attenuates CH-induced pulmonary fibrotic remodeling and EMT-associated changes

To determine the contribution of epithelial PIEZO1 to CH-associated pulmonary remodeling, we generated tamoxifen-inducible *Sftpc-Cre*^{ERT2}-mediated Piezo1 conditional-knockout (CKO) mice as previously described [11]. Efficient epithelial

Piezo1 depletion was confirmed by Piezo1/SPC immunofluorescence, Western blotting of isolated primary lung epithelial cells, and PCR genotyping (Fig. S3A–C). Following 5 weeks of CH exposure, control mice developed marked alveolar injury and collagen-rich remodeling, whereas epithelial Piezo1 deletion reduced the Smith lung injury and Ashcroft fibrosis scores (Fig. 3A, B). Consistently, lung hydroxyproline, TGF-β, and IL-6 levels were significantly lower in CH+CKO mice than in CH controls (Fig. 3C–E). Tissue immunofluorescence and Western blotting further showed that epithelial Piezo1 deletion attenuated the CH-associated loss of E-cadherin and KRT18 and the induction of Vimentin and α-SMA (Fig. 3F, G). Reduced α-SMA-positive staining in CH+CKO lungs provided additional histological support for this effect (Fig. S3D).

We next examined PIEZO1 dependence in vitro using a stable CRISPR/Cas9-edited *PIEZO1*-KO BEAS-2B cell line, with knockout efficiency confirmed at both the protein and mRNA levels (Fig. S3E). *PIEZO1* deletion markedly attenuated CH-induced EMT-associated marker changes, as demonstrated by Western blotting and immunofluorescence (Fig. 3H; Fig. S3F). At the earlier 24-h time point, hypoxia reduced *CDH1* and *TJP1* expression in both WT and *PIEZO1*-KO cells, whereas *ACTA2* and *FN1* showed minimal changes (Fig. S3G). These findings suggest that early hypoxia-associated junctional disruption is not entirely *PIEZO1* dependent and is distinct from the more pronounced PIEZO1-associated remodeling observed after prolonged exposure.

As an independent in vivo validation, AAV6-mediated *Piezo1* knockdown reduced CH-induced histological injury and collagen deposition (Fig. S4A–C). AAV6-sh*Piezo1* also decreased lung hydroxyproline and TGF-β levels, whereas the reduction in IL-6 did not reach statistical significance (Fig. S4D–F). Consistent with the CKO model, AAV6-mediated *Piezo1* knockdown preserved epithelial markers and reduced mesenchymal-marker induction, as assessed by Western blotting and immunofluorescence (Fig. S4G, H). Collectively, these complementary loss-of-function approaches support a substantial contribution of epithelial PIEZO1 to CH-associated pulmonary fibrotic remodeling and EMT-associated epithelial changes.

CH-induced mucin accumulation lies upstream of epithelial PIEZO1 and promotes pulmonary fibrotic remodeling

Previous work has shown that chronic airway epithelial hypoxia increases gel-forming mucin production and mucus concentration [2]. Consistent with this concept, CH markedly increased AB-PAS-positive material in mouse lungs, with the most prominent increase observed in acidic mucins and smaller increases in neutral and mixed mucins (Fig. 4A). MUC5AC immunoreactivity was substantially increased, whereas MUC5B showed a more modest elevation (Fig. 4B; Fig. S5A). CH-exposed BEAS-2B cells similarly exhibited increased AB-PAS-reactive material and secretion of high-molecular-weight MUC5AC (Fig. 4C, D). At the transcriptional level, CH

strongly induced MUC5AC and modestly increased MUC5B, whereas MUC1, MUC4, and MUC16 remained unchanged (Fig. 4E). PIEZO1 deletion did not significantly affect CH-induced MUC5AC or MUC5B expression, supporting the placement of mucin induction upstream of PIEZO1 (Fig. 4F).

Consistent with previous studies implicating HIF-1α in hypoxia-associated epithelial remodeling [23, 24], CH increased HIF-1α abundance, whereas HIF1A silencing reduced CH-associated PIEZO1 and MUC5AC induction (Fig. S5B, C). ChIP-qPCR further demonstrated increased HIF-1α occupancy at the MUC5AC hypoxia-response element under CH conditions (Fig. 4G). HIF1A silencing or IL-6 neutralization each partially reduced CH-induced MUC5AC and MUC5B expression, whereas combined intervention produced a further reduction (Fig. 4H, I). These findings indicate that HIF-1α-dependent hypoxia signaling and IL-6-associated inflammatory signaling make complementary contributions to gel-forming mucin induction.

To test whether airway mucin burden was sufficient to engage this pathway independently of hypoxia, mucin-coated beads were delivered intratracheally to mice, with successful mucin coating confirmed biochemically (Fig. 4J; Fig. S5D). Compared with bare beads, mucin-coated beads increased airway AB-PAS-positive material and lung PIEZO1 expression and induced EMT-associated marker changes and hydroxyproline accumulation (Fig. 4K–N). NAC attenuated mucin accumulation,

PIEZO1 induction, and the downstream remodeling phenotype. Notably, epithelial Piezo1 deletion reduced EMT-associated changes and hydroxyproline accumulation despite persistence of the introduced mucin burden (Fig. 4K, M, N), further supporting epithelial PIEZO1 as a downstream mediator of mucin-associated remodeling.

The protective effect of NAC was independently reproduced in the CH mouse model, in which intratracheal NAC reduced AB-PAS staining and attenuated EMT-associated marker changes (Fig. S5E–G). Independent validation in primary HBECs reproduced the principal directional findings: CH increased MUC5AC and MUC5B secretion, PIEZO1 expression, and EMT-associated changes, whereas NAC or the mechanosensitive-channel inhibitor GsMTx4 attenuated these responses (Fig. S5H–J). Together, these results identify mucin accumulation as an upstream component of CH-associated epithelial PIEZO1 signaling and pulmonary remodeling.

CH-CM exhibits mucus-associated rheology and enhances PIEZO1-dependent mechanical responsiveness

Having established that mucin accumulation occurs upstream of epithelial PIEZO1, we next examined whether the chronic hypoxia-conditioned epithelial secretory environment could transmit this phenotype to normoxic recipient cells. CH-CM contained substantially more MUC5AC than Nor-CM and significantly increased PIEZO1 expression in naïve BEAS-2B cells (Fig. 5A–C). The mucolytic agent N-

acetylcysteine (NAC) reduced the elevated MUC5AC abundance and attenuated CH-CM-induced PIEZO1 upregulation, without significantly altering IL-6, IL-1β, or TNF-α concentrations (Fig. 5C, D; Fig. S6B, C). Conversely, supplementation with methylcellulose (MC), a biologically inert viscous polymer, increased PIEZO1 expression under Nor-CM conditions and further enhanced PIEZO1 expression in CH-CM-treated cells (Fig. 5E). To determine whether sustained viscosity elevation also regulates PIEZO1 transcription, we measured PIEZO1 mRNA following MC treatment under normoxia. MC significantly increased PIEZO1 mRNA expression, whereas GsMTx4 partially attenuated this response without appreciably altering basal PIEZO1 expression (Fig. S6A).

CH-CM reduced E-cadherin and KRT18 and increased Vimentin and α-SMA, whereas NAC attenuated these EMT-associated changes (Fig. 5F). Methylcellulose reproduced the major directional changes induced by CH-CM (Fig. 5G), while PIEZO1 deletion markedly reduced the epithelial response to CH-CM (Fig. 5H; Fig. S6D, E). In addition, the PIEZO1 agonist Yoda1 further enhanced CH-CM-associated EMT-marker changes, and NAC partially attenuated this response (Fig. S6F).

Direct rheological measurements showed that CH-CM exhibited higher frequency-dependent storage and loss moduli than Nor-CM. Consistently, G′ and G″ at 1 Hz and apparent viscosity at 1 s^{-1} were increased in CH-CM, whereas NAC significantly

reduced each of these parameters (Fig. 5I–L). These findings demonstrate that CH alters both the elastic and viscous properties of the mucin-associated epithelial secretory environment.

We next assessed functional mechanosensitivity using cell-attached pressure-clamp recordings following CH-CM, NAC, MC, *PIEZO1*-KO, or the PIEZO1 inhibitor GsMTx4 conditioning. CH-CM and methylcellulose increased pressure-evoked currents at −40, −50, and −60 mmHg and reduced the activation threshold compared with Nor-CM (Fig. 5M–R). These changes were attenuated by NAC, PIEZO1 deletion, or GsMTx4. The proportion of mechanically responsive cells and current-inactivation kinetics showed corresponding PIEZO1-dependent changes (Fig. S8A–C). Thus, altered rheological conditioning enhances subsequent PIEZO1-dependent mechanical responsiveness.

Importantly, the principal directional findings were also reproduced under a more moderate hypoxic condition. 5% O_2 increased MUC5AC secretion, although MUC5B was significantly increased only under 1% O_2. Conditioned medium derived from 5% O_2-exposed cells increased PIEZO1 expression and induced EMT-associated changes, which were attenuated by NAC or *PIEZO1* deletion (Fig. S7A–C). Together, these results link the altered rheology of the hypoxia-conditioned secretory environment to enhanced PIEZO1-dependent mechanotransduction and epithelial remodeling.

CH-CM elicits a PIEZO1-dependent Ca^{2+} response with ER-store mobilization

Having established that altered mucus-associated rheology enhances PIEZO1-dependent mechanical responsiveness, we next examined the downstream Ca^{2+} response. Transcriptomic analyses showed enrichment of calcium-ion homeostasis and ER Ca^{2+}-handling pathways in CH-CM-treated cells and in comparisons between CH-CM-treated WT and PIEZO1-KO cells (Fig. S9A, B). Real-time Fluo-4 AM measurements showed that CH-CM induced a rapid and sustained increase in cytosolic Ca^{2+} signaling, which was markedly attenuated by PIEZO1 deletion (Fig. 6A, B). Yoda1 elicited a robust Ca^{2+} response, whereas GsMTx4 and NAC reduced the CH-CM-associated response (Fig. S9C, D, H), providing complementary pharmacological and mucus-dependence evidence.

Acute extracellular Ca^{2+} chelation with EGTA did not abolish the CH-CM-induced response. Moreover, the EGTA-resistant component was reduced by PIEZO1 deletion and enhanced by Yoda1 (Fig. S9E–G), providing initial evidence that PIEZO1 signaling is functionally coupled to intracellular Ca^{2+} stores. Because EGTA chelation alone cannot quantitatively distinguish intracellular-store mobilization from extracellular Ca^{2+} entry, we next performed nominally Ca^{2+}-free/$CaCl_2$ add-back experiments. Under Ca^{2+}-free conditions, CH-CM still elicited a substantial early cytosolic Ca^{2+} response in WT cells, whereas this response was significantly reduced

613 in PIEZO1-KO cells. Subsequent $CaCl_2$ add-back produced a secondary Ca^{2+} response
614 in CH-CM-treated WT cells, which was largely absent in Nor-CM-treated and PIEZO1-
615 KO cells (Fig. 6C). These findings indicate that CH-CM engages both an intracellular-
616 store-derived component and a PIEZO1-dependent extracellular-entry component.
617
618 Depletion of ER Ca^{2+} stores with thapsigargin markedly reduced the initial CH-CM-
619 induced cytosolic Ca^{2+} response (Fig. 6D), supporting an important contribution from
620 the ER. To directly monitor ER luminal Ca^{2+} dynamics, we used the genetically
621 encoded sensor G-CEPIA1er [17]. CH-CM accelerated the decline in G-CEPIA1er
622 fluorescence and increased the ER Ca^{2+} decay constant in WT cells, whereas both
623 changes were attenuated by *PIEZO1* deletion (Fig. 6E). Inhibition of IP3R with
624 Xestospongin-C similarly reduced the CH-CM-induced ER Ca^{2+} decay (Fig. 6F),
625 consistent with functional coupling between PIEZO1 and IP3R-associated ER Ca^{2+}
626 mobilization. Confocal colocalization with ER-Tracker verified ER targeting of G-
627 CEPIA1er, and steady-state ER luminal fluorescence was partially preserved in
628 *PIEZO1*-KO cells after CH-CM exposure (Fig. 6G). A complementary Mag-Fluo-4
629 AM assay [25] also showed a reduced low-affinity organellar Ca^{2+} signal after CH-CM
630 treatment, with partial restoration following *PIEZO1* deletion (Fig. S9I).
631
632 Together, these data demonstrate that CH-CM evokes a composite PIEZO1-dependent
633 Ca^{2+} response. Although extracellular Ca^{2+} entry contributes to the overall signal, IP3R-

associated ER-store mobilization represents a prominent intracellular amplification step. We therefore next examined whether this ER-derived component was transmitted to mitochondria through ER–mitochondrial contact sites.

PIEZO1 signaling promotes MAM remodeling and ER-to-mitochondrial Ca^{2+} transfer

Having identified IP3R-associated ER-store mobilization as a prominent component of the PIEZO1-dependent Ca^{2+} response, we next examined whether this signal was transmitted to mitochondria through ER–mitochondrial contact sites. GO cellular-component analysis of CH-CM-treated WT versus PIEZO1-KO cells showed enrichment of mitochondrial, ER membrane, and mitochondria-associated ER membrane terms (Fig. S10A). Concurrently, we assessed mitochondrial Ca^{2+} using Rhod-2 AM [26] with MitoTracker. CH-CM treatment triggered a rapid and robust elevation in mitochondrial Ca^{2+}, whereas this uptake was significantly blunted in *PIEZO1*-KO cells (Fig. 7A, B). To verify the involvement of mitochondria-associated membranes (MAMs)—the specialized contact sites facilitating ER-mitochondria coupling [19, 27, 28], we performed ER-Tracker and MitoTracker colocalization analysis. CH-CM significantly increased ER–mitochondria colocalization, and this effect was reduced in *PIEZO1*-KO cells (Fig. 7C, D). Transmission electron microscopy (TEM) further revealed shortening of the ER–mitochondria gap distance after CH-CM stimulation, whereas *PIEZO1*-KO cells maintained a larger inter-

655 organelle distance (Fig. 7E), consistent with increased MAM formation in response to
656 CH-CM. Together, these results indicate that PIEZO1 signaling promotes the
657 association of the IP3R2–GRP75–VDAC1 MAM tethering machinery.
658
659 Next, we identified the molecular bridge mediating this tethering. Mechanistically, CH-
660 CM upregulated the expression of the tethering protein GRP75 in a PIEZO1-dependent
661 manner (Fig. 7H). IF analysis showed increased spatial association of IP3R2 (ER Ca^{2+}
662 channel), GRP75 (cytosolic tether), and VDAC1 (outer mitochondrial membrane
663 channel) after CH-CM treatment, whereas these changes were attenuated in *PIEZO1*-
664 KO cells (Fig. 7G). Consistent with these observations, Co-immunoprecipitation (Co-
665 IP) showed increased association of GRP75 with VDAC1 and IP3R2 in CH-CM–
666 treated cells, and these inducible interactions were reduced by PIEZO1 depletion (Fig.
667 7F).
668
669 To determine whether this complex was functionally required for mitochondrial Ca^{2+}
670 loading, we selected a validated GRP75-targeting siRNA (Fig. S10B). GRP75
671 knockdown reduced CH-CM-induced mitochondrial Rhod-2 fluorescence and blunted
672 the additional response to Yoda1 (Fig. 7I). Similarly, inhibition of mitochondrial Ca^{2+}
673 uptake with the MCU inhibitor Ru360 reduced both CH-CM- and Yoda1-associated
674 mitochondrial Ca^{2+} accumulation (Fig. 7J). The fast intracellular Ca^{2+} chelator BAPTA-
675 AM produced a greater reduction in mitochondrial Ca^{2+} signal than EGTA-AM (Fig.

676 S10C), consistent with Ca^{2+} transfer through a spatially restricted ER–mitochondrial
677 microdomain.
678
679 Consistent with the known consequences of sustained mitochondrial Ca^{2+} loading [29,
680 30], CH-CM increased mitochondrial superoxide and total cellular ROS and promoted
681 mitochondrial membrane depolarization. These changes were attenuated by PIEZO1
682 deletion or GsMTx4 and were enhanced by Yoda1 (Fig. S10D–F).
683
684 Collectively, these findings support a model in which PIEZO1-dependent ER Ca^{2+}
685 mobilization is coupled to MAM remodeling and IP3R2–GRP75–VDAC1-mediated
686 mitochondrial Ca^{2+} transfer, leading to mitochondrial Ca^{2+} overload and early
687 mitochondrial stress.
688
689
690 ***PIEZO1 amplifies CH-CM-induced mtDNA release, cGAS-STING signaling and***
691 ***EMT-associated changes***
692 Sustained elevation of mitochondrial Ca^{2+} is known to precipitate mitochondrial
693 dysfunction and subsequent mitochondrial permeability transition pore (mPTP)
694 opening [29, 30]. We next assessed mPTP opening using the calcein-AM/$CoCl_2$
695 quenching assay. CH-CM induced a marked reduction in mitochondrial calcein signal

696 in WT cells, indicating increased mPTP opening, whereas this response was attenuated
697 in *PIEZO1*-KO cells (Fig. 8A, C).
698
699 The opening of the mPTP facilitates the leakage of mitochondrial contents into the
700 cytosol, including mtDNA [31]. Confocal imaging of dsDNA and MitoTracker showed
701 increased extranuclear, extra-mitochondrial dsDNA puncta after CH-CM treatment,
702 whereas this phenotype was reduced in *PIEZO1*-KO cells (Fig. 8B, D). To quantify this
703 release, we further performed subcellular fractionation on BEAS-2B cells to isolate
704 cytosolic and mitochondrial components. qPCR analysis of the cytosolic fraction
705 revealed a marked elevation of the mtDNA signature genes *MT-ND1* and *MT-ND2* [32]
706 following CH-CM treatment. Conversely, this cytosolic mtDNA accumulation was
707 significantly blunted in *PIEZO1*-KO cells (Fig. 8E).
708
709 Because cytosolic mtDNA can activate cGAS and stimulate 2′3′-cGAMP production,
710 we next asked whether PIEZO1-dependent mitochondrial injury was linked to cGAS-
711 STING signaling. We observed a marked increase in intracellular 2′3′-cGAMP in CH-
712 CM–treated cells, and this increase was attenuated in *PIEZO1*-KO cells (Fig. 8F),
713 supporting activation of cGAS downstream of PIEZO1-dependent mitochondrial stress.
714
715 cGAMP acts as a second messenger to activate STING, which recruits and
716 phosphorylates TBK1, subsequently activating downstream IRF3 and NF-κB pathways.

CH-CM increased cGAS abundance and STING phosphorylation, together with phosphorylation of TBK1, IRF3, and NF-κB. Each of these responses was attenuated, although not completely abolished, by PIEZO1 deletion (Fig. 8G; Fig. S11A). *In vivo*, CH similarly increased cGAS and p-STING/STING in whole-lung lysates, whereas epithelial *Piezo1* CKO reduced these responses (Fig. 8H). Double immunofluorescence further demonstrated increased p-STING signal within KRT18-positive epithelial regions after CH exposure, with a significant reduction in CH+CKO lungs (Fig. 8I). These findings provide cell-resolved evidence for an epithelial-intrinsic STING component, while not excluding additional immune-cell-mediated amplification in the intact lung. Increased p-STING/STING and its attenuation by NAC or GsMTx4 were also observed in primary HBECs (Fig. S11E). In the hypoxia-independent mucin-coated bead model, STING phosphorylation was increased, whereas NAC treatment or epithelial Piezo1 deletion attenuated this response (Fig. S11F).

Pharmacological epistasis further positioned cGAS–STING downstream of PIEZO1. In CH-CM-treated *PIEZO1*-KO cells, the STING agonist SR717 restored TBK1/IRF3/NF-κB signaling and partially restored EMT-associated marker changes. Conversely, Yoda1 enhanced downstream signaling and EMT-associated changes in WT cells, whereas the cGAS inhibitor Ru.521 or the STING inhibitor H-151 attenuated these effects (Fig. 8J; Fig. S11B). Under normoxic conditions, Yoda1 alone was sufficient to increase STING phosphorylation and induce EMT-associated marker

changes; these effects were reduced by PIEZO1 deletion or H-151 (Fig. S11C, D). In vivo, Yoda1 aggravated CH-associated EMT-marker changes, whereas H-151 markedly attenuated this response (Fig. 8K).

We finally examined whether epithelial PIEZO1 signaling could influence fibroblasts through a paracrine mechanism. Conditioned medium derived from CH-exposed WT epithelial cells increased *ACTA2*, *COL1A1*, and *FN1* expression in recipient human lung fibroblasts compared with conditioned medium from normoxic epithelial cells. These responses were significantly attenuated when the conditioned medium was derived from CH-exposed *PIEZO1*-KO epithelial cells (Fig. 8L–O). Thus, epithelial PIEZO1 contributes to the generation of a fibroblast-activating secretory milieu, although the responsible soluble mediators and the stability of the resulting fibroblast phenotype remain to be defined.

Collectively, these findings support a sequential pathway in which PIEZO1-dependent ER–mitochondrial Ca^{2+} transfer promotes mitochondrial injury, mPTP opening, mtDNA release, and epithelial cGAS–STING activation, with downstream effects on both epithelial remodeling and epithelial-to-fibroblast paracrine signaling.

Discussion

In this study, we identify a mucus-associated mechanotransduction pathway linking chronic hypoxia (CH) to epithelial dysfunction and pulmonary fibrotic remodeling. Rather than viewing CH solely as a metabolic or inflammatory stress, our data indicate that CH also remodels the epithelial microenvironment by increasing mucin burden and altering secretory-milieu rheology. HIF-1α/IL-6 perturbation, mucin-coated bead delivery, NAC-mediated mucolysis, and epithelial PIEZO1 loss-of-function position mucin accumulation upstream of PIEZO1-dependent mechanotransduction. Direct rheology showed that CH-CM had higher storage modulus, loss modulus, and apparent viscosity, whereas pressure-clamp recordings demonstrated enhanced PIEZO1-dependent mechanically activated currents. Downstream, PIEZO1 engages a composite Ca^{2+} response in which extracellular entry remains detectable, whereas IP3R-associated ER-store mobilization serves as a prominent intracellular amplification step coupled to ER–mitochondrial Ca^{2+} transfer, mitochondrial injury, mtDNA release, and epithelial cGAS–STING activation. Thus, our findings extend rather than replace HIF-centered models of hypoxic injury by adding a biophysical signaling branch downstream of epithelial stress.

These findings should be interpreted within the broader network of hypoxia-responsive and mechanosensitive pathways that regulate pulmonary fibrotic remodeling. Hypoxia can directly perturb epithelial homeostasis through HIF-1α-dependent ER stress, apoptosis, and altered epithelial fate decisions, providing PIEZO1-independent routes

779 to epithelial injury and fibrotic remodeling. In parallel, PIEZO1 represents only one
780 component of the pulmonary mechanosensing machinery. Integrin–FAK signaling,
781 YAP/TAZ-dependent mechanotransduction, and TRPV4 have each been implicated in
782 fibrotic remodeling [33, 34]. Of particular relevance to the present study, abnormal
783 extracellular viscosity has also been shown to activate integrin-β1/vinculin/FAK
784 signaling and promote pulmonary fibrogenesis [35]. These pathways may operate in
785 parallel with, or converge upon, the mucus–PIEZO1 axis identified here. Thus, we view
786 mucus-associated PIEZO1 signaling as one experimentally supported biophysical
787 branch within a broader hypoxia-responsive mechano-fibrotic network, rather than as
788 the exclusive mechanism linking chronic hypoxia to pulmonary fibrotic remodeling.
789
790 A central question in pulmonary mechanobiology is how a non-solid, gel-like interface
791 modulates a mechanically gated channel in the absence of overt tissue stretch. Previous
792 lung studies have primarily examined solid-matrix stiffness, cyclic stretch, ventilator-
793 associated deformation, or force sensing by mesenchymal and myofibroblast
794 populations as upstream stimuli for PIEZO1 [10, 36, 37]. In parallel, airway mucus
795 studies have established that increasing mucus concentration increases its elastic and
796 viscous moduli and impairs mucus transport. Our data support an additional possibility:
797 that CH-induced mucus accumulation itself provides a local viscoelastic environment
798 that enhances epithelial PIEZO1. This interpretation is consistent with the broader
799 concept that PIEZO1 can respond to viscoelastic properties in addition to simple
800 stiffness [38]. In our model, NAC reduced CH-CM storage modulus, loss modulus, and

apparent viscosity and attenuated PIEZO1 upregulation and EMT-associated changes, whereas methylcellulose reproduced the key phenotype. Mucin-coated beads also induced PIEZO1-associated remodeling under normoxia. Moreover, CH-CM or methylcellulose conditioning increased pressure-evoked currents and lowered activation thresholds in a PIEZO1-dependent manner, consistent with enhanced PIEZO1-dependent mechanosensitivity following exposure to an altered rheological environment [15]. Together, these results support the idea that altered mucus rheology is not merely an epiphenomenon of hypoxic injury but can act as a proximal mechanical amplifier of lung epithelial signaling.

Our results agree with Mikami et al. [2] that chronic epithelial hypoxia increases gel-forming mucin burden, but the predominant mucin isoform differed between experimental systems. Mikami et al. observed MUC5B-dominant mucus hyperconcentration in well-differentiated primary human airway epithelia, whereas MUC5AC was the more strongly induced mucin in our mouse lungs and submerged BEAS-2B model, with a smaller increase in MUC5B and no broad induction of the membrane-associated mucins MUC1, MUC4, or MUC16 (Fig. 4B, D, E; Fig. S5A, H). This discrepancy likely reflects the distinct pathological contexts modeled by different experimental systems. While MUC5B is the primary homeostatic mucin in distal airways, MUC5AC upregulation is a hallmark of pathological goblet cell metaplasia often associated with severe inflammation and fibrosis [39, 40]. Indeed, recent studies

822 demonstrated that BEAS-2B cells readily differentiate into MUC5AC-secreting goblet-
823 like cells under stress stimuli [41-43], supporting the validity of our *in vitro*
824 observations. Importantly, both MUC5AC and MUC5B accumulation lead to the
825 formation of a hyperviscous, viscoelastic gel. Furthermore, MUC5AC is known to form
826 stiffer, more tightly tethered mucus networks than MUC5B [44, 45], potentially
827 generating a more robust mechanical shear stress to stimulate PIEZO1 in the context of
828 fibrotic remodeling. Mechanistically, HIF1α silencing reduced mucin expression, and
829 ChIP-qPCR demonstrated increased HIF-1α occupancy at the MUC5AC hypoxia-
830 response element (Fig. 4G), consistent with promoter studies in human bronchial
831 epithelial cells [46]. IL-6 neutralization produced an additional partial reduction, and
832 combined HIF1A silencing and IL-6 blockade exerted a greater effect, indicating
833 convergence of direct hypoxia signaling and inflammatory amplification (Fig. 4H, I).
834 Importantly, *PIEZO1* deletion did not reduce CH-induced mucin expression, and
835 epithelial *Piezo1* CKO attenuated bead-induced downstream remodeling without
836 eliminating the introduced mucin burden. These directional results place mucin
837 accumulation upstream of PIEZO1 rather than within a PIEZO1-dependent feedback
838 loop.
839
840 The human datasets and tissue analyses provide complementary but context-dependent
841 support for the disease relevance of this pathway. COPD-associated datasets were
842 included because advanced COPD commonly combines epithelial hypoxic stress,

mucus accumulation, and airway remodeling, rather than because COPD represents a prototypical interstitial fibrotic disease. This distinction is also important for mucin interpretation. In idiopathic pulmonary fibrosis (IPF), MUC5B is strongly linked to disease susceptibility and bronchiolized epithelial remodeling, most notably through the MUC5B promoter variant rs35705950 and the accumulation of MUC5B-rich epithelium in honeycomb cysts [47, 48]. By contrast, our model is hypoxia-driven rather than genetically MUC5B-driven. In this setting, MUC5AC may be particularly relevant because it is a stress-inducible mucin closely associated with HIF-1α–dependent goblet cell metaplasia and abnormal mucus accumulation under hypoxic conditions [49]. Accordingly, we do not interpret our findings as opposing the established role of MUC5B in IPF. Rather, we propose that MUC5B may be more closely related to disease susceptibility and epithelial lineage context, whereas hypoxia-inducible MUC5AC may function as a pathological accelerator that increases local mucus viscoelasticity and thereby amplifies PIEZO1-dependent mechanotransduction during disease progression.

An important interpretive issue is whether the epithelial phenotype reflects generalized injury caused by severe hypoxia or a separable mucus–PIEZO1-dependent signaling component. Exposure to 1% O_2 produced a modest late reduction in metabolic activity, while LDH release remained unchanged, indicating sublethal metabolic stress without extensive loss of plasma-membrane integrity. At an earlier time point, reductions in TEER, CDH1, and TJP1 preceded broad induction of ACTA2 and FN1, suggesting that

junctional dysfunction develops before the more established EMT-associated phenotype. Direct hypoxic injury therefore contributes to the epithelial response but does not fully account for its delayed progression.

Crucially, transferring CH-conditioned medium (CH-CM) to normoxic recipient cells was sufficient to induce PIEZO1 upregulation and EMT-associated changes and conditioned medium generated at 5% O_2 reproduced the principal MUC5AC–PIEZO1-associated response, indicating that the hypoxia-conditioned secretory milieu can transmit the phenotype. In addition, methylcellulose conditioning and mucin-coated beads reproduced key elements of the phenotype without exposing recipient cells or mice to hypoxia. NAC and genetic PIEZO1 deletion interrupted the pathway at different levels: NAC reduced mucin abundance and rheological parameters, whereas PIEZO1 deletion preserved the upstream mucin burden but attenuated downstream Ca^{2+} signaling and remodeling. NAC did not broadly reduce the measured soluble cytokines, supporting a mucin-network contribution, although its antioxidant and additional biochemical effects cannot be excluded. Previous work in differentiated human tracheobronchial epithelia similarly showed that mucoactive agents, including NAC, alter mucin-associated properties and mucociliary transport [50]. This aligns with the paradigm proposed by Oliva et al. [38], who identified PIEZO1 as a sophisticated sensor capable of detecting substrate viscoelasticity beyond simple stiffness. Together, these experiments support a contribution of mucin-associated rheology to epithelial

886 PIEZO1 signaling, but do not establish that all CH-CM effects arise from mucins; other
887 macromolecules and extracellular particles may also contribute. Intriguingly, these
888 findings offer a perspective for clinical translation, particularly regarding drug
889 repurposing. NAC has been traditionally administered systemically as a biochemical
890 antioxidant in fibrotic lung diseases with mixed or controversial clinical outcomes [51-
891 53]. In this context, our data provide a complementary, mechanistically distinct
892 perspective: we used NAC primarily as a mucolytic to relieve the pathological
893 viscoelastic mechanical load at the lung epithelial surface. This "mechanical
894 decoupling" markedly attenuated PIEZO1 upregulation and EMT-associated changes
895 in our models, contrasting with the traditional view of NAC as a redox-targeting therapy
896 and suggesting that its potential impact may be context dependent—particularly in
897 hypoxia-associated, mucus-enriched states where aberrant lung epithelial surface
898 mechanics can act upstream of mechanotransduction.
899
900 Mechanistically, our findings support a serial Ca^{2+}-amplification model downstream of
901 PIEZO1. PIEZO1 is canonically a mechanically activated cation channel [13], and the
902 Ca^{2+}-free/add-back experiments confirmed a detectable extracellular-entry component.
903 Nevertheless, persistence of an early response under Ca^{2+}-free conditions, its
904 attenuation following ER-store depletion, and the complementary G-CEPIA1er and
905 Xestospongin-C results identify IP3R-associated ER-store mobilization as a prominent
906 intracellular amplification step (Fig. 6). This aligns with recent signal amplification

907 models in which PIEZO1 activation is functionally coupled to internal ER stores to
908 facilitate endogenous Ca^{2+} release via IP3R channels [17, 54]. Building upon this
909 concept, we identified MAMs as the structural bridge that converts this ER Ca^{2+} efflux
910 into mitochondrial dysfunction. PIEZO1 activation promoted the assembly of the
911 IP3R2–GRP75–VDAC1 tethering complex, creating a direct conduit for Ca^{2+} transfer
912 (Fig. 7). The greater effect of BAPTA-AM than EGTA-AM further supports Ca^{2+}
913 transfer through a spatially restricted microdomain (Fig. S10C). These observations
914 establish functional coupling between PIEZO1 signaling and MAM-mediated Ca^{2+}
915 transfer, but do not determine whether PIEZO1 itself resides at the ER–mitochondrial
916 interface; both a plasma-membrane-initiated serial circuit [17] and an intracellular
917 PIEZO1 pool described in epithelial cells [55] remain plausible.
918
919 Mitochondrial Ca^{2+} loading was followed by oxidative stress, membrane depolarization,
920 mPTP opening, cytosolic MT-ND1/MT-ND2 accumulation, and increased cGAMP,
921 providing a sequential link between organelle dysfunction and cGAS–STING signaling.
922 The epithelial monoculture experiments, normoxic Yoda1 gain-of-function analysis,
923 PIEZO1 loss-of-function, cGAS/STING inhibition, and SR717 rescue collectively
924 support an epithelial-autonomous component of this pathway. The increased p-STING
925 signal within KRT18-positive cells further localizes part of the in vivo response to the
926 epithelial compartment. This interpretation is consistent with the observation that
927 cytosolic mtDNA can activate cGAS-dependent pathological programs in primary IPF

928 alveolar epithelial cells [56]. However, DNA released from injured epithelium can
929 activate macrophage STING and IL-6–STAT3 signaling during airway fibrosis [57].
930 Moreover, conditioned medium from CH-exposed epithelial cells increased fibroblast
931 ACTA2, COL1A1, and FN1 expression, whereas PIEZO1 deficiency in donor
932 epithelial cells attenuated this effect (Fig. 8L-O). A similar epithelial-to-fibroblast
933 relationship has been demonstrated for aberrant intermediate alveolar epithelial cells
934 that generate a profibrotic secretome [58]. Epithelial PIEZO1–cGAS–STING signaling
935 may therefore function as one component of a broader epithelial–immune–
936 mesenchymal network rather than as the exclusive origin of tissue-level fibrosis.
937
938 Several limitations of our study warrant consideration. First, although this study
939 focused on epithelial mechanotransduction, PIEZO1 in macrophages and endothelial
940 cells may also shape fibrotic remodeling [59-61], raising the possibility of a
941 multicellular positive-feedback circuit that shapes the fibrotic niche. Second, most
942 mechanistic experiments were performed in BEAS-2B cells under static submerged
943 culture and severe hypoxia. Validation under 5% O_2 and in primary HBECs improved
944 cross-model robustness, but these systems do not reproduce donor heterogeneity,
945 epithelial polarization, mucociliary clearance, or breathing-associated cyclic strain [62].
946 Future studies using patient-derived air-liquid interface cultures, precision-cut lung
947 slices, and lung-on-chip platforms will be important to define how mucus
948 viscoelasticity interacts with dynamic mechanical cues. Third, although we functionally

linked PIEZO1 to ER Ca^{2+} mobilization and MAM remodeling, we did not directly visualize PIEZO1 localization at the ER or MAM interface in the hypoxic setting. While McHugh et al. previously reported ER-localized PIEZO1 in other cell types [55], it remains unclear whether CH induces the translocation of PIEZO1 from the plasma membrane to intracellular organelles, or instead activates a pre-existing intracellular PIEZO1 pool. Future work employing super-resolution imaging will be required to delineate the spatiotemporal trafficking of PIEZO1 during hypoxic remodeling.

In conclusion, this study supports a hypoxia–mucin–PIEZO1 mechanotransduction framework that links remodeling of the epithelial secretory environment to pulmonary fibrotic remodeling. By integrating mucin-loading models, direct rheological characterization, pressure-clamp electrophysiology, and lung epithelial *PIEZO1* loss-of-function approaches, we identify abnormal mucus rheology as an active biophysical signal that enhances PIEZO1-dependent mechanical responsiveness rather than merely representing a passive consequence of lung injury. Mechanistically, PIEZO1-associated ER Ca^{2+} mobilization and MAM-mediated mitochondrial Ca^{2+} transfer connect extracellular biophysical remodeling to mitochondrial injury, mtDNA release, epithelial cGAS–STING activation, EMT-associated changes, and fibroblast-activating paracrine signaling. This mechanistic continuum expands the current understanding of how chronic hypoxia is translated into multicellular lung remodeling. Clinically, the findings provide a rationale for targeting multiple levels of this pathway—including

mucin burden and rheology, PIEZO1-dependent mechanotransduction, ER–mitochondrial Ca^{2+} coupling, and cGAS–STING signaling—and may inform mechanism-based therapeutic strategies for hypoxia- and mucus-enriched fibrotic lung disease.

Abbreviations

CH: Chronic hypoxia; CH-CM: Chronic hypoxia-conditioned medium; cGAS: Cyclic GMP-AMP synthase; CKO: Conditional knockout; COPD: Chronic obstructive pulmonary disease; EMT: Epithelial-mesenchymal transition; ER: Endoplasmic reticulum; GRP75: Glucose-regulated protein 75; HIF: Hypoxia-inducible factor; HBEC: Human bronchial epithelial cell; IP3R2: Inositol 1,4,5-trisphosphate receptor type 2; KO: Knockout; MAMs: Mitochondria-associated membranes; MC: Methylcellulose; mPTP: Mitochondrial permeability transition pore; mtDNA: Mitochondrial DNA; NAC: N-acetylcysteine; Nor: Normoxia; Nor-CM: Normoxia-conditioned medium; PF: Pulmonary fibrosis; STING: Stimulator of interferon genes; TBK1: TANK-binding kinase 1; VDAC1: Voltage-dependent anion channel 1; WT: Wild-type.

Acknowledgements

Funding: This work was supported by the National Science Fund for Young Scholars (No.82500138 and 82200061), Shanghai Leading Talent Program of Eastern Talent Plan (CG2109-2), the National Natural Science Foundation of China (No. 82370088,

82470090 and 82470089), and the National Key Research and Development Program of China (No. 2026ZD0555800).

Author Contributions

XPW, PJ, LLZ, and ZLL contributed equally to this work. XPW performed most of the experiments, analyzed data, and interpreted results. SYH, SQL, and MZ conceptualized the study and were responsible for funding acquisition, resources, and supervision. XPW, PJ, and LLZ were responsible for data analysis and the methodology. YJY, YFD, ZLL, XDW, XXD, and RHH were responsible for the investigation. PJ, LLZ, and ZLL were responsible for sample collection.

Data Availability Statement

The public single-cell RNA sequencing datasets analyzed in this study were obtained from the GEO under accession numbers GSE158942, GSE227508, GSE273062, GSE135893, GSE136831, and GSE190889. The RNA-seq datasets generated and analyzed during the current study have been deposited in the GEO under the accession number GSE313903. Additional data supporting the findings of this study are available from the corresponding author upon reasonable request.

Conflict-of-interest statement

The authors have declared that no competing interests exist.

References

1. Liu GY, Budinger GRS, Dematte JE. Advances in the management of idiopathic pulmonary fibrosis and progressive pulmonary fibrosis. BMJ. 2022;377:e066354.
2. Mikami Y, Grubb BR, Rogers TD, Dang H, Asakura T, Kota P, et al. Chronic airway epithelial hypoxia exacerbates injury in muco-obstructive lung disease through mucus hyperconcentration. Sci Transl Med. 2023;15(699):eabo7728.
3. Mall MA, Danahay H, Boucher RC. Emerging Concepts and Therapies for Mucoobstructive Lung Disease. Ann Am Thorac Soc. 2018;15(Suppl 3):S216.
4. Wan M, Yu Q, Xu F, You LX, Liang X, Kang Ren K, et al. Novel hypoxia-induced HIF-1alpha activation in asthma pathogenesis. Respir Res. 2024;25(1):287.
5. Prabhakar NR, Peng YJ, Nanduri J. Hypoxia-inducible factors and obstructive sleep apnea. J Clin Invest. 2020;130(10):5042.
6. Luks AM, Hackett PH. Medical Conditions and High-Altitude Travel. N Engl J Med. 2022;386(4):364.
7. Goodwin J, Choi H, Hsieh MH, Neugent ML, Ahn JM, Hayenga HN, et al. Targeting Hypoxia-Inducible Factor-1alpha/Pyruvate Dehydrogenase Kinase 1 Axis by Dichloroacetate Suppresses Bleomycin-induced Pulmonary Fibrosis. Am J Respir Cell Mol Biol. 2018;58(2):216.
8. Lamouille S, Xu J, Derynck R. Molecular mechanisms of epithelial-mesenchymal transition. Nat Rev Mol Cell Biol. 2014;15(3):178.
9. Higgins DF, Kimura K, Bernhardt WM, Shrimanker N, Akai Y, Hohenstein B, et al. Hypoxia promotes fibrogenesis in vivo via HIF-1 stimulation of epithelial-to-mesenchymal transition. J Clin Invest. 2007;117(12):3810.
10. Xu L, Li T, Cao Y, He Y, Shao Z, Liu S, et al. PIEZO1 mediates periostin+ myofibroblast activation and pulmonary fibrosis in mice. J Clin Invest. 2025;135(11).
11. Fang XZ, Li M, Wang YX, Zhang P, Sun MM, Xu JX, et al. Mechanosensitive ion channel Piezo1 mediates mechanical ventilation-exacerbated ARDS-associated pulmonary fibrosis. J Adv Res. 2023;53:175.
12. Lim M, Park S, Joo YH, Kim SE, Ham MH, Kim T, et al. Piezo1-mediated mechanotransduction regulates the translational activity, function and lung pathogenicity of group 2 innate lymphoid cells. Signal Transduct Target Ther. 2025;10(1):269.
13. Coste B, Mathur J, Schmidt M, Earley TJ, Ranade S, Petrus MJ, et al. Piezo1 and Piezo2 are essential components of distinct mechanically activated cation channels. Science. 2010;330(6000):55.
14. Markovetz MR, Subramani DB, Kissner WJ, Morrison CB, Garbarine IC, Ghio A, et al. Endotracheal tube mucus as a source of airway mucus for rheological study. Am J Physiol Lung Cell Mol Physiol. 317. United States2019. p. L498.

15. MAG. O, Ciccone G, Flaschner G, Luo J, Voigt JL, Romani P, et al. Piezo1 regulates the mechanotransduction of soft matrix viscoelasticity. Nat Commun. 2025;16(1):9155.
16. Lin Z, Xu G, Lu X, Wang H, Lu F, Xia X, et al. Piezo1 exacerbates inflammation-induced cartilaginous endplate degeneration by activating mitochondrial fission via the Ca(2+)/CaMKII/Drp1 axis. Aging Cell. 2025;24(4):e14440.
17. Santana Nunez D, Malik AB, Lee Q, Ahn SJ, Coctecon-Murillo A, Lazarko D, et al. Piezo1 induces endothelial responses to shear stress via soluble adenylyl Cyclase-IP(3)R2 circuit. iScience. 2023;26(5):106661.
18. Li Y, Zhu L, Cai MX, Wang ZL, Zhuang M, Tan CY, et al. TGR5 suppresses cGAS/STING pathway by inhibiting GRP75-mediated endoplasmic reticulum-mitochondrial coupling in diabetic retinopathy. Cell Death Dis. 2023;14(9):583.
19. Missiroli S, Patergnani S, Caroccia N, Pedriali G, Perrone M, Previati M, et al. Mitochondria-associated membranes (MAMs) and inflammation. Cell Death Dis. 2018;9(3):329.
20. Limberis MP, Vandenberghe LH, Zhang L, Pickles RJ, Wilson JM. Transduction efficiencies of novel AAV vectors in mouse airway epithelium in vivo and human ciliated airway epithelium in vitro. Mol Ther. 2009;17(2):294.
21. Markovetz MR, Subramani DB, Kissner WJ, Morrison CB, Garbarine IC, Ghio A, et al. Endotracheal tube mucus as a source of airway mucus for rheological study. Am J Physiol Lung Cell Mol Physiol. 2019;317:L498.
22. Li J, Qi F, Su H, Zhang C, Zhang Q, Chen Y, et al. GRP75-facilitated Mitochondria-associated ER Membrane (MAM) Integrity controls Cisplatin-resistance in Ovarian Cancer Patients. Int J Biol Sci. 2022;18(7):2914.
23. Zhou G, Dada LA, Wu M, Kelly A, Trejo H, Zhou Q, et al. Hypoxia-induced alveolar epithelial-mesenchymal transition requires mitochondrial ROS and hypoxia-inducible factor 1. Am J Physiol Lung Cell Mol Physiol. 2009;297(6):L1120.
24. Palazon A, Goldrath AW, Nizet V, Johnson RS. HIF transcription factors, inflammation, and immunity. Immunity. 2014;41(4):518.
25. Rossi AM, Taylor CW. Reliable measurement of free Ca(2+) concentrations in the ER lumen using Mag-Fluo-4. Cell Calcium. 2020;87:102188.
26. Song Z, Song H, Liu D, Yan B, Wang D, Zhang Y, et al. Overexpression of MFN2 alleviates sorafenib-induced cardiomyocyte necroptosis via the MAM-CaMKIIdelta pathway in vitro and in vivo. Theranostics. 2022;12(3):1267.
27. Gong Y, Lu X, Wang X, Wang Y, Shen Z, Gao Y, et al. Mitochondrial Tumor Suppressor 1A Attenuates Myocardial Infarction Injury by Maintaining the Coupling Between Mitochondria and Endoplasmic Reticulum. Circulation. 2025;152(3):183.
28. Arruda AP, Pers BM, Parlakgul G, Guney E, Inouye K, Hotamisligil GS. Chronic enrichment of hepatic endoplasmic reticulum-mitochondria contact leads to mitochondrial dysfunction in obesity. Nat Med. 2014;20(12):1427.

29. Li Y, Zhu L, Cai MX, Wang ZL, Zhuang M, Tan CY, et al. TGR5 supresses cGAS/STING pathway by inhibiting GRP75-mediated endoplasmic reticulum-mitochondrial coupling in diabetic retinopathy. Cell Death Dis. 2023;14(9):583.
30. Bernardi P, Gerle C, Halestrap AP, Jonas EA, Karch J, Mnatsakanyan N, et al. Identity, structure, and function of the mitochondrial permeability transition pore: controversies, consensus, recent advances, and future directions. Cell Death Differ. 2023;30(8):1869.
31. Kerkhofs M, La Rovere R, Welkenhuysen K, Janssens A, Vandenberghe P, Madesh M, et al. BIRD-2, a BH4-domain-targeting peptide of Bcl-2, provokes Bax/Bak-independent cell death in B-cell cancers through mitochondrial Ca(2+)-dependent mPTP opening. Cell Calcium. 2021;94:102333.
32. Ouyang W, Wang S, Yan D, Wu J, Zhang Y, Li W, et al. The cGAS-STING pathway-dependent sensing of mitochondrial DNA mediates ocular surface inflammation. Signal Transduct Target Ther. 2023;8:371.
33. Lagares D, Busnadiego O, Garcia-Fernandez RA, Kapoor M, Liu S, Carter DE, et al. Inhibition of focal adhesion kinase prevents experimental lung fibrosis and myofibroblast formation. Arthritis Rheum. 2012;64(5):1653.
34. Rahaman SO, Grove LM, Paruchuri S, Southern BD, Abraham S, Niese KA, et al. TRPV4 mediates myofibroblast differentiation and pulmonary fibrosis in mice. J Clin Invest. 2014;124(12):5225.
35. Chen J, Guo K, Xie L, Zhi Y, Hong J, Chen C. Abnormal matrix viscosity promotes the progression of radiation-induced pulmonary fibrosis through integrin-beta1/vinculin/FAK pathway in the presclerotic stage. Cell Signal. 2026;137:112184.
36. Xu Y, Huang Y, Cheng X, Hu B, Jiang D, Wu L, et al. Mechanotransductive receptor Piezo1 as a promising target in the treatment of fibrosis diseases. Front Mol Biosci. 2023;10:1270979.
37. Lin Y, Wen D, Chen K, Hu Z, Ho C, Liu Y, et al. Piezo1 and tissue fibrosis: insights into its role and potential for modulation. Burns Trauma. 2025;13:tkaf054.
38. M AGO, Ciccone G, Flaschner G, Luo J, Voigt JL, Romani P, et al. Piezo1 regulates the mechanotransduction of soft matrix viscoelasticity. Nat Commun. 2025;16(1):9155.
39. Curran DR, Cohn L. Advances in mucous cell metaplasia: a plug for mucus as a therapeutic focus in chronic airway disease. Am J Respir Cell Mol Biol. 2010;42(3):268.
40. Young HW, Williams OW, Chandra D, Bellinghausen LK, Perez G, Suarez A, et al. Central role of Muc5ac expression in mucous metaplasia and its regulation by conserved 5' elements. Am J Respir Cell Mol Biol. 2007;37(3):273.
41. Zhu H, Leng J, Ju R, Qu S, Tian J, Leng H, et al. Advantages of pulsed electric field ablation for COPD: Excellent killing effect on goblet cells. Bioelectrochemistry. 2024;158:108726.

42. Wu X, Zhang G, Du X. Cigarette Smoke Extract Induces MUC5AC Expression Through the ROS/ IP3R/Ca(2+) Pathway in Calu-3 Cells. Int J Chron Obstruct Pulmon Dis. 2024;19:1635.
43. Park SH, Gong JH, Choi YJ, Kang MK, Kim YH, Kang YH. Kaempferol Inhibits Endoplasmic Reticulum Stress-Associated Mucus Hypersecretion in Airway Epithelial Cells And Ovalbumin-Sensitized Mice. PLoS One. 2015;10(11):e0143526.
44. Carpenter J, Wang Y, Gupta R, Li Y, Haridass P, Subramani DB, et al. Assembly and organization of the N-terminal region of mucin MUC5AC: Indications for structural and functional distinction from MUC5B. Proc Natl Acad Sci U S A. 2021;118(39).
45. Kesimer M. Mucins MUC5AC and MUC5B in the Airways: MUCing around Together. Am J Respir Crit Care Med. 2022;206(9):1055.
46. Zhou X, Tu J, Li Q, Kolosov VP, Perelman JM. Hypoxia induces mucin expression and secretion in human bronchial epithelial cells. Transl Res. 2012;160(6):419.
47. Seibold MA, Wise AL, Speer MC, Steele MP, Brown KK, Loyd JE, et al. A common MUC5B promoter polymorphism and pulmonary fibrosis. N Engl J Med. 2011;364(16):1503.
48. Hancock LA, Hennessy CE, Solomon GM, Dobrinskikh E, Estrella A, Hara N, et al. Muc5b overexpression causes mucociliary dysfunction and enhances lung fibrosis in mice. Nat Commun. 2018;9(1):5363.
49. Polosukhin VV, Cates JM, Lawson WE, Milstone AP, Matafonov AG, Massion PP, et al. Hypoxia-inducible factor-1 signalling promotes goblet cell hyperplasia in airway epithelium. J Pathol. 2011;224(2):203.
50. Seagrave J, Albrecht HH, Hill DB, Rogers DF, Solomon G. Effects of guaifenesin, N-acetylcysteine, and ambroxol on MUC5AC and mucociliary transport in primary differentiated human tracheal-bronchial cells. Respir Res. 2012;13:98.
51. Huang H, Chen M, Liu F, Wu H, Wang J, Chen J, et al. N-acetylcysteine therapeutically protects against pulmonary fibrosis in a mouse model of silicosis. Biosci Rep. 2019;39(7).
52. Sakamoto S, Kataoka K, Kondoh Y, Kato M, Okamoto M, Mukae H, et al. Pirfenidone plus inhaled N-acetylcysteine for idiopathic pulmonary fibrosis: a randomised trial. Eur Respir J. 2021;57(1).
53. Yahia Z, Yahia A, Abdelaziz T. N-acetylcysteine Clinical Applications. Cureus. 2024;16(10):e72252.
54. Velasco-Estevez M, Rolle SO, Mampay M, Dev KK, Sheridan GK. Piezo1 regulates calcium oscillations and cytokine release from astrocytes. Glia. 2020;68(1):145.
55. McHugh BJ, Buttery R, Lad Y, Banks S, Haslett C, Sethi T. Integrin activation by Fam38A uses a novel mechanism of R-Ras targeting to the endoplasmic reticulum. J Cell Sci. 2010;123(Pt 1):51.

56. Schuliga M, Kanwal A, Read J, Blokland KEC, Burgess JK, Prele CM, et al. A cGAS-dependent response links DNA damage and senescence in alveolar epithelial cells: a potential drug target in IPF. Am J Physiol Lung Cell Mol Physiol. 2021;321(5):L859.
57. Chen Y, Yang C, Miao Y, Shi D, Li X, Tian S, et al. Macrophage STING signaling promotes fibrosis in benign airway stenosis via an IL6-STAT3 pathway. Nat Commun. 2025;16:289.
58. Hoffman ET, Shah A, Barboza WR, Rodriguez LR, Dherwani R, Dooley PE, et al. Aberrant intermediate alveolar epithelial cells promote pathogenic activation of lung fibroblasts in preclinical fibrosis models. Nat Commun. 2025;16:8710.
59. Solis AG, Bielecki P, Steach HR, Sharma L, Harman CCD, Yun S, et al. Mechanosensation of cyclical force by PIEZO1 is essential for innate immunity. Nature. 2019;573(7772):69.
60. Friedrich EE, Hong Z, Xiong S, Zhong M, Di A, Rehman J, et al. Endothelial cell Piezo1 mediates pressure-induced lung vascular hyperpermeability via disruption of adherens junctions. Proc Natl Acad Sci U S A. 2019;116(26):12980.
61. Wang Z, Chen J, Babicheva A, Jain PP, Rodriguez M, Ayon RJ, et al. Endothelial upregulation of mechanosensitive channel Piezo1 in pulmonary hypertension. Am J Physiol Cell Physiol. 2021;321(6):C1010.
62. Pezzulo AA, Starner TD, Scheetz TE, Traver GL, Tilley AE, Harvey BG, et al. The air-liquid interface and use of primary cell cultures are important to recapitulate the transcriptional profile of in vivo airway epithelia. Am J Physiol Lung Cell Mol Physiol. 2011;300(1):L25.

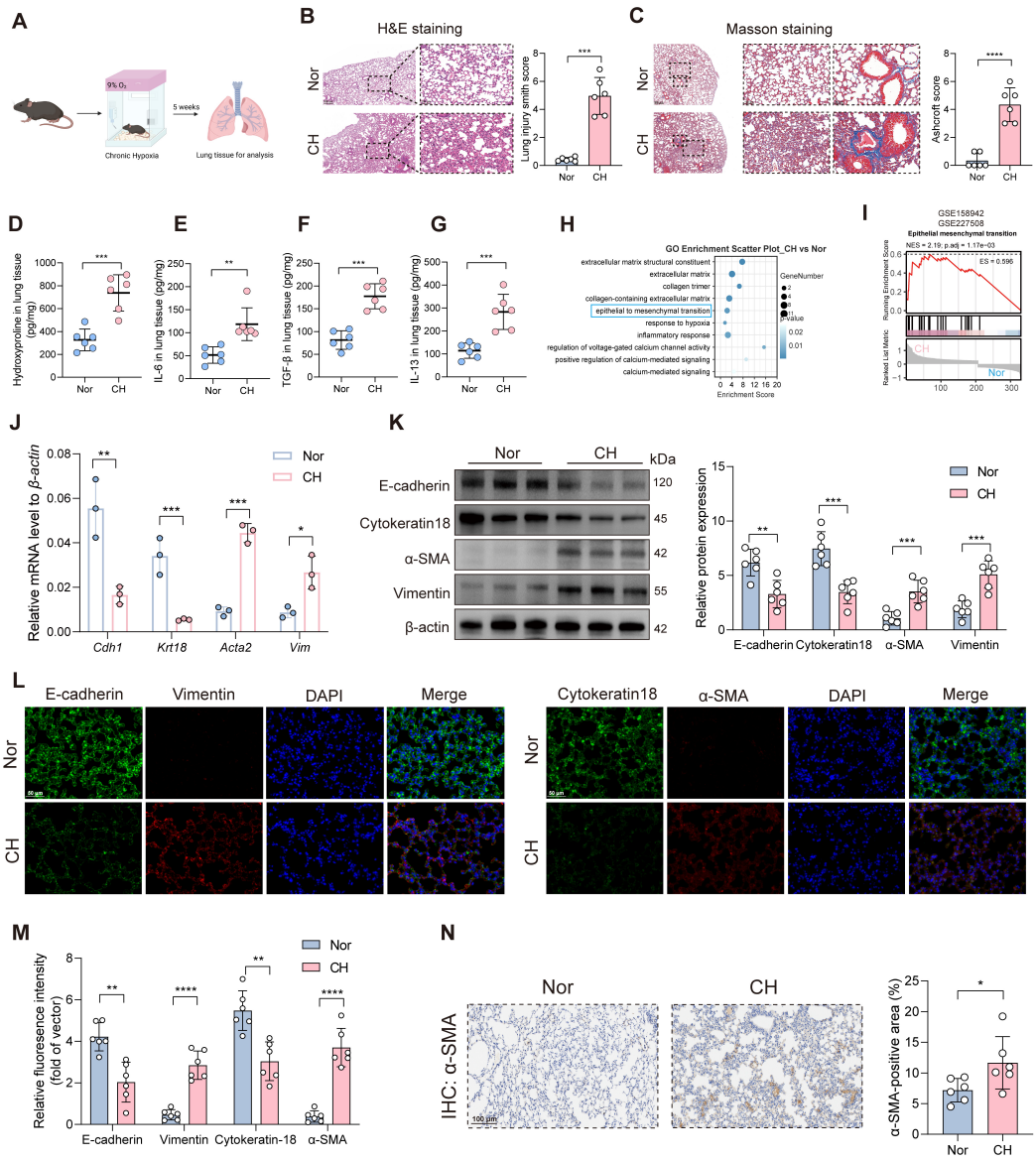

A
9% O2
5 weeks
Chronic Hypoxia
Lung tissue for analysis
B
H&E staining
Nor
CH
Lung injury smith score
Nor
CH
C
Masson staining
Nor
CH
Ashcroft score
Nor
CH
D
Hydroxyproline in lung tissue (pg/mg)
Nor
CH
E
IL-6 in lung tissue (pg/mg)
Nor
CH
F
TGF-β in lung tissue (pg/mg)
Nor
CH
G
IL-13 in lung tissue (pg/mg)
Nor
CH
H
GO Enrichment Scatter Plot_CH vs Nor
extracellular matrix structural constituent
extracellular matrix
collagen trimer
collagen-containing extracellular matrix
epithelial to mesenchymal transition
response to hypoxia
inflammatory response
regulation of voltage-gated calcium channel activity
positive regulation of calcium-mediated signaling
calcium-mediated signaling
GeneNumber
p.value
Enrichment Score
I
GSE158942
GSE227508
Epithelial mesenchymal transition
NES = 2.19, p.adj = 1.17e-03
ES = 0.596
Running Enrichment Score
Ranked List Metric
CH
Nor
J
Relative mRNA level to β-actin
Nor
CH
Cdh1
Krt18
Acta2
Vim
K
Nor
CH
kDa
E-cadherin
Cytokeratin18
α-SMA
Vimentin
β-actin
120
45
42
55
42
Relative protein expression
Nor
CH
E-cadherin
Cytokeratin18
α-SMA
Vimentin
L
E-cadherin
Vimentin
DAPI
Merge
Cytokeratin18
α-SMA
DAPI
Merge
Nor
CH
M
Relative fluorescence intensity (fold of vector)
Nor
CH
E-cadherin
Vimentin
Cytokeratin-18
α-SMA
N
Nor
CH
IHC: α-SMA
α-SMA-positive area (%)
Nor
CH

Figure 1. Chronic hypoxia induces pulmonary fibrotic remodeling with EMT-associated changes. **(A)** Schematic diagram of chronic hypoxia (CH) mouse model. **(B, C)** Representative H&E staining and Lung injury Smith score **(B)**, Masson's trichrome staining and Ashcroft fibrosis score **(C)** of lung tissues from normoxia (Nor) and CH groups. (n = 6 mice/group). **(D–G)** Lung tissue concentrations of hydroxyproline **(D)**, IL-6 **(E)**, TGF-β **(F)**, and IL-13 (**G)** (n = 6). **(H)** Gene Ontology enrichment analyses of bulk RNA-seq data (GSE313903) comparing CH and Nor. **(I)** GSEA of the EMT signature based on integrated analysis of published scRNA-seq datasets from COPD patients (GSE158942) and chronic hypoxia-treated primary HBECs (GSE227508). **(J)** RT-qPCR analysis of epithelial (*Cdh1*, *Krt18*) and mesenchymal (*Acta2*, *Vim*) mRNA expression in lung tissues (n = 3). **(K)** Western blot and densitometric quantification of EMT-related proteins. β-actin served as a loading control (n = 6). **(L, M)** Representative immunofluorescence images **(L)** and relative fluorescence quantification **(M)** of E-cadherin/Vimentin and Cytokeratin18/α-SMA in lung sections (n = 6). Nuclei were counterstained with DAPI. **(N)** Representative α-SMA immunohistochemistry (IHC) and quantification of the α-SMA-positive area (n = 6). Scale bars are indicated in the images. Data are presented as mean ± SD. *$P <$ 0.05, **$P < 0.01$, ***$P < 0.001$, ****$P < 0.0001$ (Two-tailed unpaired Student's *t*-test).

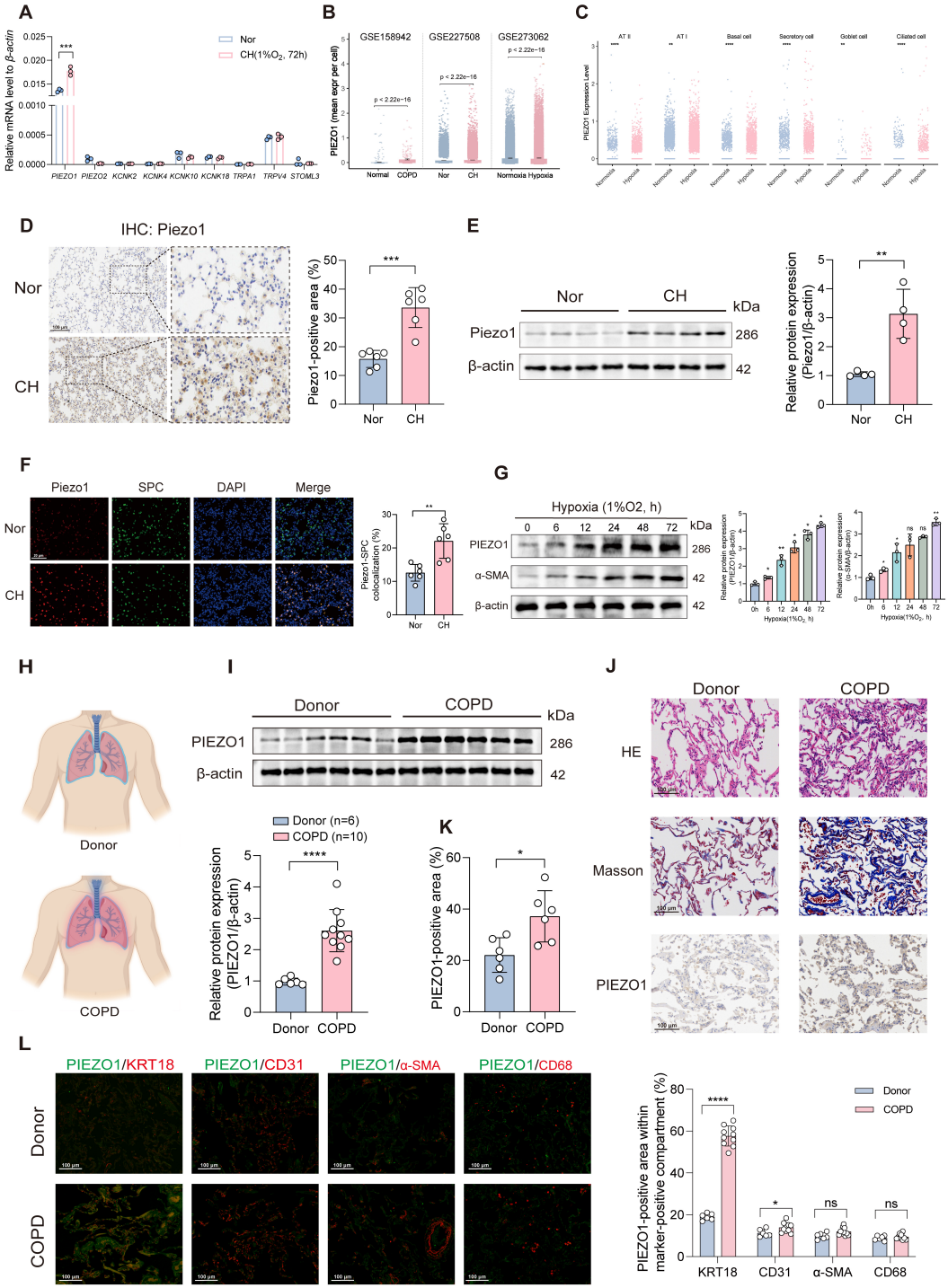

A
Relative mRNA level to β-actin
Nor
CH(1%O2, 72h)
PIEZO1 PIEZO2 KCNK2 KCNK4 KCNK10 KCNK18 TRPA1 TRPV4 STOML3
B
GSE158942
GSE227508
GSE273062
PIEZO1 (mean expr per cell)
Normal COPD Nor CH Normoxia Hypoxia
C
AT II
AT I
Basal cell
Secretory cell
Goblet cell
Ciliated cell
PIEZO1 Expression Level
D
IHC: Piezo1
Nor
CH
Piezo1-positive area (%)
E
Nor
CH
kDa
Piezo1
β-actin
286
42
Relative protein expression (Piezo1/β-actin)
F
Piezo1
SPC
DAPI
Merge
Piezo1-SPC colocalization (%)
G
Hypoxia (1%O2, h)
0 6 12 24 48 72
PIEZO1
α-SMA
β-actin
H
Donor
COPD
I
Donor
COPD
PIEZO1
β-actin
Donor (n=6)
COPD (n=10)
Relative protein expression (PIEZO1/β-actin)
J
HE
Masson
PIEZO1
K
PIEZO1-positive area (%)
L
PIEZO1/KRT18
PIEZO1/CD31
PIEZO1/α-SMA
PIEZO1/CD68
PIEZO1-positive area within marker-positive compartment (%)
KRT18 CD31 α-SMA CD68
ns

Figure 2. **Chronic hypoxia upregulates PIEZO1 expression in lung epithelial cells.** **(A)** RT-qPCR analysis of mechanosensitive ion channel transcripts in BEAS-2B cells under normoxia (Nor) or chronic hypoxia (CH, 1% O_2, 72 h) (n = 3 independent experiments). **(B)** Single-cell expression distributions of human *PIEZO1* or rat *Piezo1* in three independent publicly available datasets: primary airway basal cells from control subjects and patients with COPD (GSE158942), normoxic and CH-exposed human bronchial epithelial cells (GSE227508), and normoxic and hypoxia-exposed rat lungs (GSE273062). **(C)** PIEZO1 expression across epithelial subsets identified from integrated human epithelial datasets (GSE158942 and GSE227508). **(D)** Representative Piezo1 IHC images and quantification of Piezo1-positive area in mouse lung sections (n = 6). **(E)** Western blot analysis and quantification of Piezo1 in mouse whole-lung homogenates (n = 6). **(F)** Representative IF images of PIEZO1 (red) and SPC (green) in mouse lung sections, with quantification of PIEZO1/SPC colocalization (n = 6). Nuclei were stained with DAPI (blue). **(G)** Western blot analysis and quantification of PIEZO1 and α-SMA in BEAS-2B cells across a hypoxia time course (n = 3). **(H)** Schematic representation of the human lung-tissue cohort. **(I)** Western blot analysis and quantification of PIEZO1 in lung homogenates from non-COPD control donors (n = 6) and patients with COPD (n = 10). **(J, K)** Representative H&E, Masson's trichrome, and PIEZO1 IHC images with quantification of PIEZO1-positive area in human lung sections (n = 6). **(L)** Representative double-immunofluorescence images of PIEZO1 with KRT18, CD31, α-SMA, or CD68 in control-donor and COPD lung tissues, with quantification of the PIEZO1-positive area within each marker-positive cellular compartment. Multiple non-overlapping fields were averaged to obtain one value for each biological specimen. Scale bars are indicated in the images. Data are presented as mean ± SD. Data in **(A, L)** were analyzed using two-way ANOVA followed by Šídák's multiple-comparisons test; data in **(D–F, I, K)** were analyzed using two-tailed unpaired Student's *t*-tests, with Welch's correction where appropriate; data in **(G)** were analyzed using one-way ANOVA followed by Dunnett's multiple-comparisons test; and single-cell comparisons in **(B, C)** were performed using two-sided Wilcoxon rank-sum tests. *$P < 0.05$, ** $P < 0.01$, *** $P < 0.001$, **** $P < 0.0001$; ns, not significant.

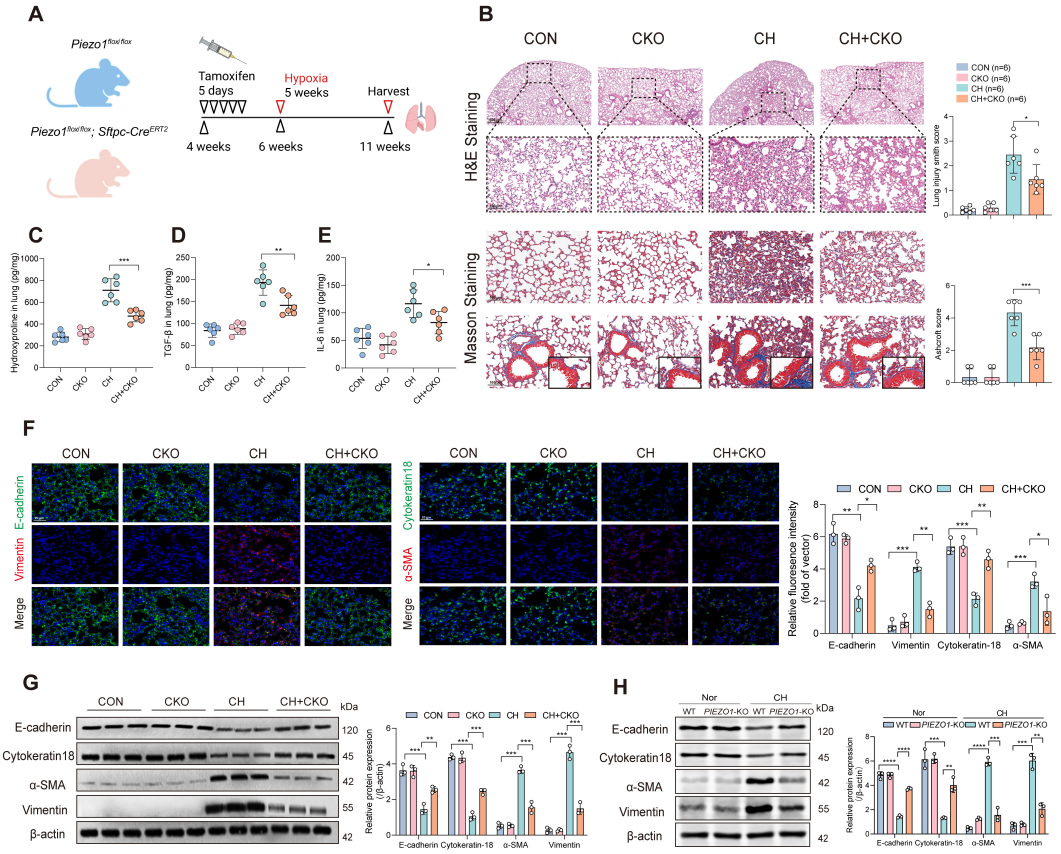

A
Piezo1flox/flox
Piezo1flox/flox; Sftpc-CreERT2
Tamoxifen
5 days
Hypoxia
5 weeks
Harvest
4 weeks
6 weeks
11 weeks
B
CON
CKO
CH
CH+CKO
H&E Staining
Masson Staining
Lung injury score
Ashcroft score
C
Hydroxyproline in lung (ng/mg)
D
TGF-β in lung (pg/mg)
E
IL-6 in lung (pg/mg)
F
E-cadherin
Vimentin
Cytokeratin18
α-SMA
Merge
Relative fluorescence intensity (fold of vector)
G
kDa
β-actin
Relative protein expression (/β-actin)
H
Nor
CH
WT
PIEZO1-KO

Figure 3. **Lung epithelial PIEZO1 deficiency attenuates CH-induced pulmonary fibrotic remodeling and EMT-associated changes**. **(A)** Schematic of inducible lung epithelial-specific *Piezo1* knockout (*Piezo1*$^{flox/flox}$; *Sftpc*-Cre^{ERT2}) mice and the experimental timeline. **(B)** H&E and Masson's trichrome staining of lung sections from Control (CON), CKO, CH, and CH+CKO groups, with Smith injury and Ashcroft fibrosis scores (n = 6 mice/group). **(C–E)** Lung homogenate levels of hydroxyproline **(C)**, TGF-β **(D)**, and IL-6 **(E)** (n = 6). **(F)** Representative immunofluorescence images and fluorescence-intensity quantification of E-cadherin/Vimentin and Cytokeratin-18/α-SMA in mouse lung sections. Nuclei were counterstained with DAPI (n = 3). **(G)** Representative Western blots and densitometric quantification of E-cadherin, Cytokeratin-18, α-SMA, and Vimentin in mouse lung homogenates (n = 3). **(H)** Representative Western blots and densitometric quantification of EMT-associated proteins in WT and *PIEZO1*-KO BEAS-2B cells exposed to normoxia (Nor) or CH. β-actin served as the loading control (n = 3 independent experiments). Scale bars are indicated in the images. Statistical comparisons were performed using one-way or two-way ANOVA followed by Tukey's multiple-comparisons test, as appropriate. *$P < 0.05$, ** $P < 0.01$, *** $P < 0.001$, **** $P < 0.0001$; ns, not significant.

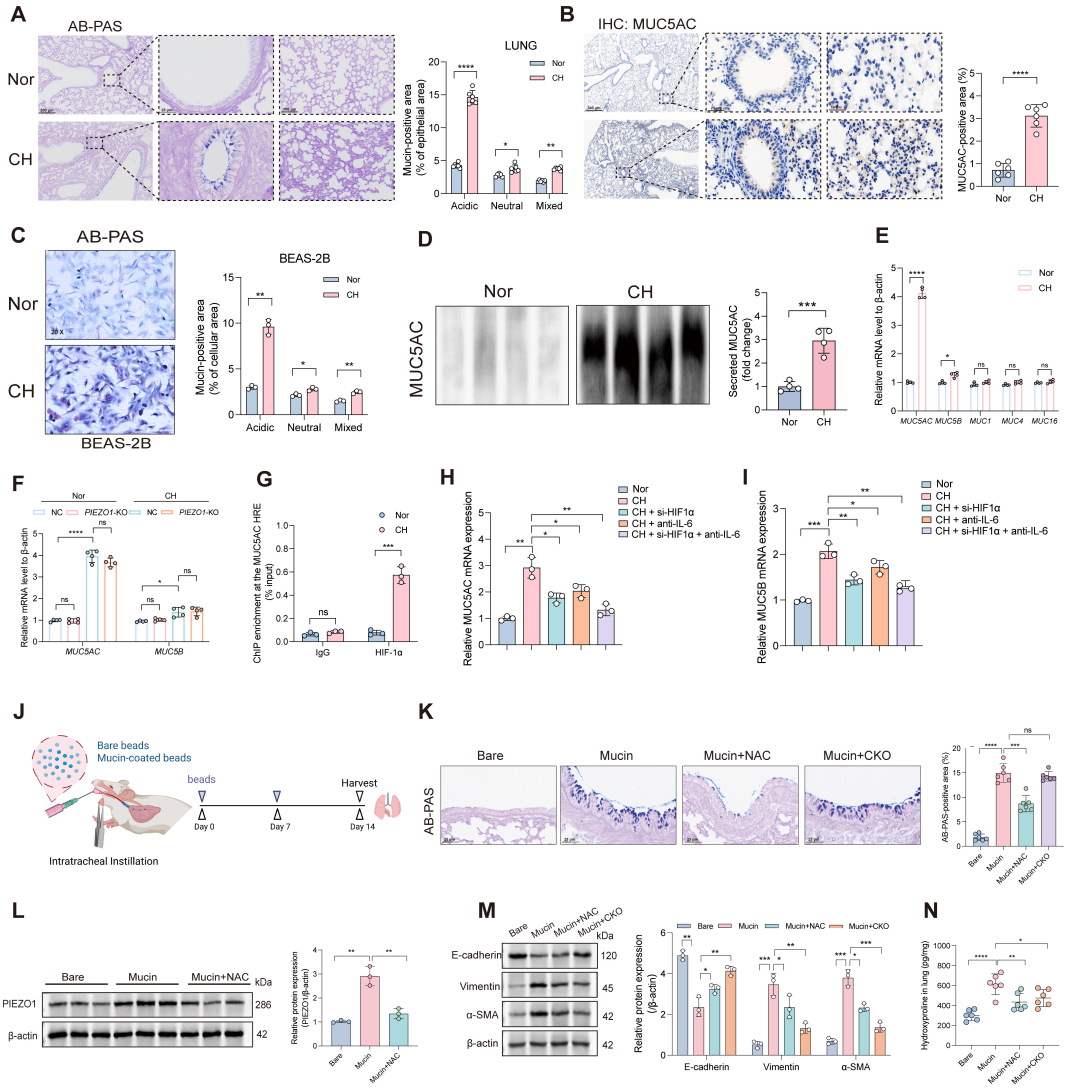

A
AB-PAS
Nor
CH
LUNG
Nor
CH
Mucin-positive area (% of epithelial area)
Acidic
Neutral
Mixed
B
IHC: MUC5AC
MUC5AC-positive area (%)
C
AB-PAS
BEAS-2B
Mucin-positive area (% of cellular area)
D
MUC5AC
Secreted MUC5AC (fold change)
E
Relative mRNA level to β-actin
MUC5AC
MUC5B
MUC1
MUC4
MUC16
F
NC
PIEZO1-KO
Relative mRNA level to β-actin
G
ChIP enrichment at the MUC5AC HRE (% input)
IgG
HIF-1α
H
Relative MUC5AC mRNA expression
CH + si-HIF1α
CH + anti-IL-6
CH + si-HIF1α + anti-IL-6
I
Relative MUC5B mRNA expression
J
Bare beads
Mucin-coated beads
beads
Harvest
Day 0
Day 7
Day 14
Intratracheal Instillation
K
Bare
Mucin
Mucin+NAC
Mucin+CKO
AB-PAS
AB-PAS-positive area (%)
L
PIEZO1
β-actin
kDa
286
42
Relative protein expression (PIEZO1/β-actin)
M
E-cadherin
Vimentin
α-SMA
β-actin
120
45
42
Relative protein expression (/β-actin)
N
Hydroxyproline in lung (pg/mg)

Figure 4. CH-induced mucin accumulation lies upstream of lung epithelial PIEZO1 and promotes pulmonary remodeling.

(A) Representative AB-PAS staining and quantification of acidic, neutral, and mixed mucin-positive areas in lung sections from normoxic (Nor) and CH-exposed mice (n = 6 mice/group). Dashed boxes indicate enlarged regions. **(B)** MUC5AC immunohistochemistry and positive-area quantification in mouse lungs (n = 6 mice/group). **(C)** AB-PAS staining and mucin-subtype quantification in BEAS-2B cells under Nor or CH conditions (n = 3 independent experiments). **(D)** Agarose-gel immunoblotting and densitometric quantification of secreted high-molecular-weight MUC5AC (n = 4). **(E)** RT-qPCR analysis of *MUC5AC, MUC5B, MUC1, MUC4,* and *MUC16* in BEAS-2B cells (n = 3). **(F)** *MUC5AC* and *MUC5B* expression in control and *PIEZO1*-KO cells under Nor or CH conditions (n = 4). **(G)** ChIP-qPCR analysis of HIF-1α occupancy at the *MUC5AC* hypoxia-response element; IgG served as the negative control (n = 3). **(H, I)** *MUC5AC* **(H)** and *MUC5B* **(I)** expression following HIF-1α silencing, IL-6 neutralization, or combined treatment under CH (n = 3). **(J)** Schematic of intratracheal bare- or mucin-coated bead administration on days 0 and 7, with lung collection on day 14. **(K)** Representative AB-PAS staining and positive-area quantification in bare-bead, mucin-bead, mucin+NAC, and mucin+CKO groups (n = 6 mice/group). **(L)** Western blotting and quantification of PIEZO1 after bare-bead, mucin-bead, or mucin+NAC administration (n = 3 mice/group). **(M)** Western blotting and quantification of E-cadherin, Vimentin, and α-SMA in the bead model (n = 3 mice/group). **(N)** Lung hydroxyproline content (n = 6 mice/group). β-actin served as the loading control. Scale bars are indicated in the images. Data are mean ± SD. Two-group comparisons were analyzed using two-tailed unpaired Student's *t*-tests; multiple-group comparisons were analyzed using one- or two-way ANOVA followed by appropriate multiple-comparisons tests. **P* < 0.05, ** *P* < 0.01, *** *P* < 0.001, **** *P* < 0.0001; ns, not significant.

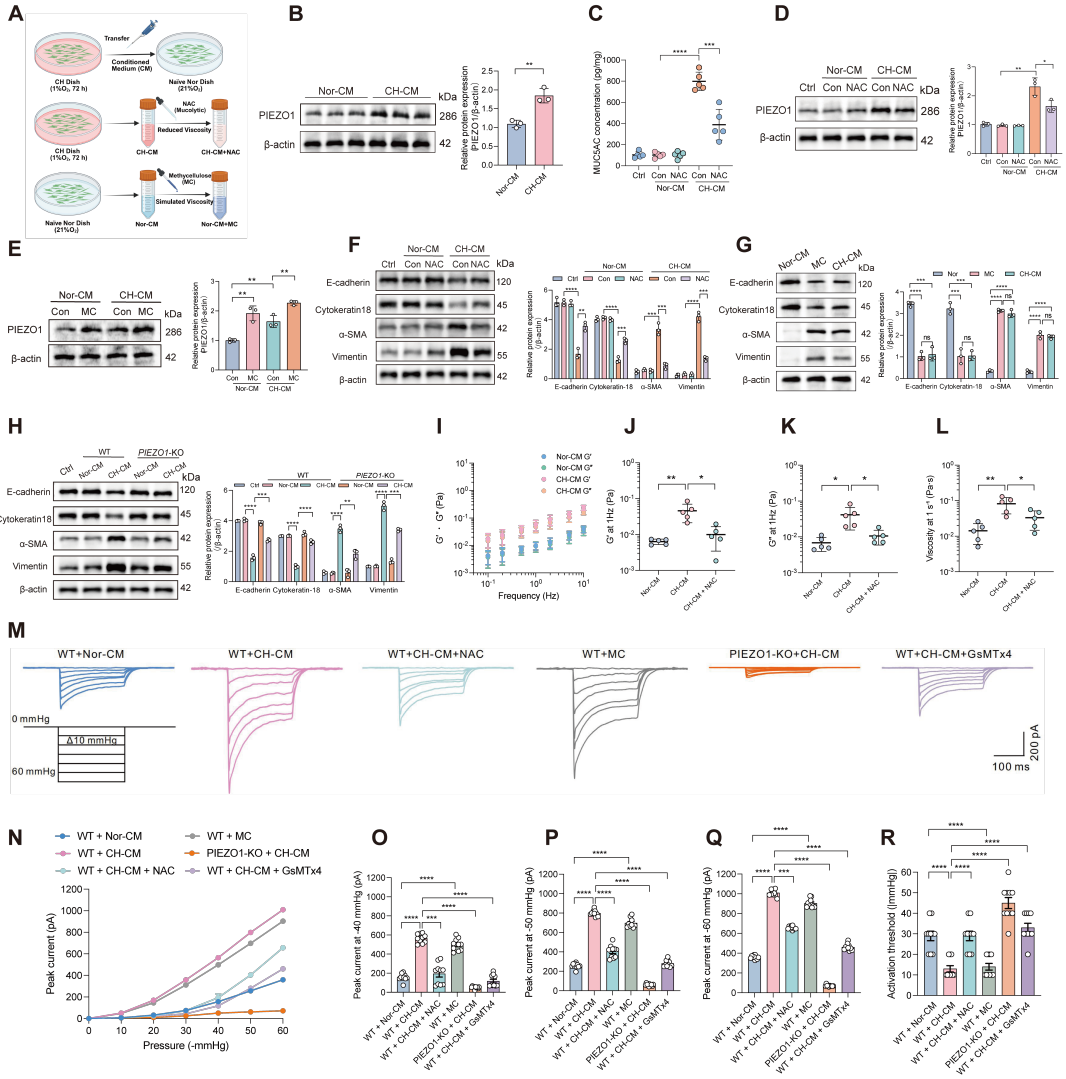

A
Transfer
Conditioned Medium (CM)
CH Dish (1%O2, 72 h)
Naive Nor Dish (21%O2)
NAC (Mucolytic)
Reduced Viscosity
CH-CM
CH-CM+NAC
Methylcellulose (MC)
Simulated Viscosity
Nor-CM
Nor-CM+MC
B
Nor-CM
CH-CM
kDa
PIEZO1
β-actin
286
42
Relative protein expression (PIEZO1/β-actin)
C
MUC5AC concentration (pg/mg)
Ctrl
Con
NAC
Con NAC
Nor-CM
CH-CM
D
E
MC
F
E-cadherin
Cytokeratin18
α-SMA
Vimentin
120
45
55
G
H
WT
PIEZO1-KO
I
J
K
L
M
WT+Nor-CM
WT+CH-CM
WT+CH-CM+NAC
WT+MC
PIEZO1-KO+CH-CM
WT+CH-CM+GsMTx4
0 mmHg
Δ10 mmHg
60 mmHg
200 pA
100 ms
N
WT + Nor-CM
WT + CH-CM
WT + CH-CM + NAC
WT + MC
PIEZO1-KO + CH-CM
WT + CH-CM + GsMTx4
Peak current (pA)
Pressure (-mmHg)
O
Peak current at -40 mmHg (pA)
P
Peak current at -50 mmHg (pA)
Q
Peak current at -60 mmHg (pA)
R
Activation threshold (|mmHg|)

Figure 5. Altered mucus-associated rheology enhances PIEZO1-dependent mechanical responsiveness and lung epithelial remodeling.

(A) Schematic of conditioned-medium transfer, NAC-mediated mucolysis, and methylcellulose (MC)-based rheological conditioning. **(B)** PIEZO1 Western blotting and quantification in BEAS-2B cells exposed to Nor-CM or CH-CM (n = 3 independent experiments). **(C)** MUC5AC concentrations in untreated controls (Ctrl) or Nor-CM/CH-CM treated with vehicle control (Con) or NAC (n = 5). **(D)** PIEZO1 Western blotting and quantification under the corresponding NAC-treatment conditions (n = 3). **(E)** PIEZO1 Western blotting and quantification after Nor-CM or CH-CM treatment with or without MC supplementation (n = 3). **(F)** Western blotting and quantification of EMT-associated proteins following Nor-CM or CH-CM exposure with or without NAC (n = 3). **(G)** Western blotting and quantification of EMT-associated proteins in cells exposed to Nor-CM, Nor-CM+MC, or CH-CM (n = 3). **(H)** Western blotting and quantification of EMT-associated proteins in WT and *PIEZO1*-KO cells exposed to Nor-CM or CH-CM (n = 3). **(I)** Frequency-dependent storage modulus (G′) and loss modulus (G″) of Nor-CM and CH-CM (n = 5 independently prepared CM batches). **(J–L)** G′ at 1 Hz **(J)**, G″ at 1 Hz **(K)**, and apparent viscosity at 1 s^{-1} **(L)** in Nor-CM, CH-CM, and NAC-treated CH-CM (n = 5 independently prepared CM batches). **(M)** Representative families of pressure-evoked currents recorded in the cell-attached configuration after the indicated conditioning treatments. Negative-pressure steps were applied from 0 to −60 mmHg in 10-mmHg increments. **(N)** Pressure–current relationships (n = 10 technically valid cells/group from three independent cell preparations). **(O–Q)** Peak currents evoked at −40 **(O)**, −50 **(P)**, and −60 mmHg **(Q)** (n = 10 cells/group). **(R)** Activation thresholds, expressed as the absolute magnitude of negative pressure (n = 10 cells/group). β-actin served as the loading control. Data are presented as mean ± SD for biochemical and rheological assays and electrophysiological analyses. Pressure–current relationships were analyzed using repeated-measures two-way ANOVA; other multiple-group comparisons were analyzed using one- or two-way ANOVA followed by appropriate multiple-comparisons tests. *$P < 0.05$, ** $P < 0.01$, *** $P < 0.001$, **** $P < 0.0001$; ns, not significant.

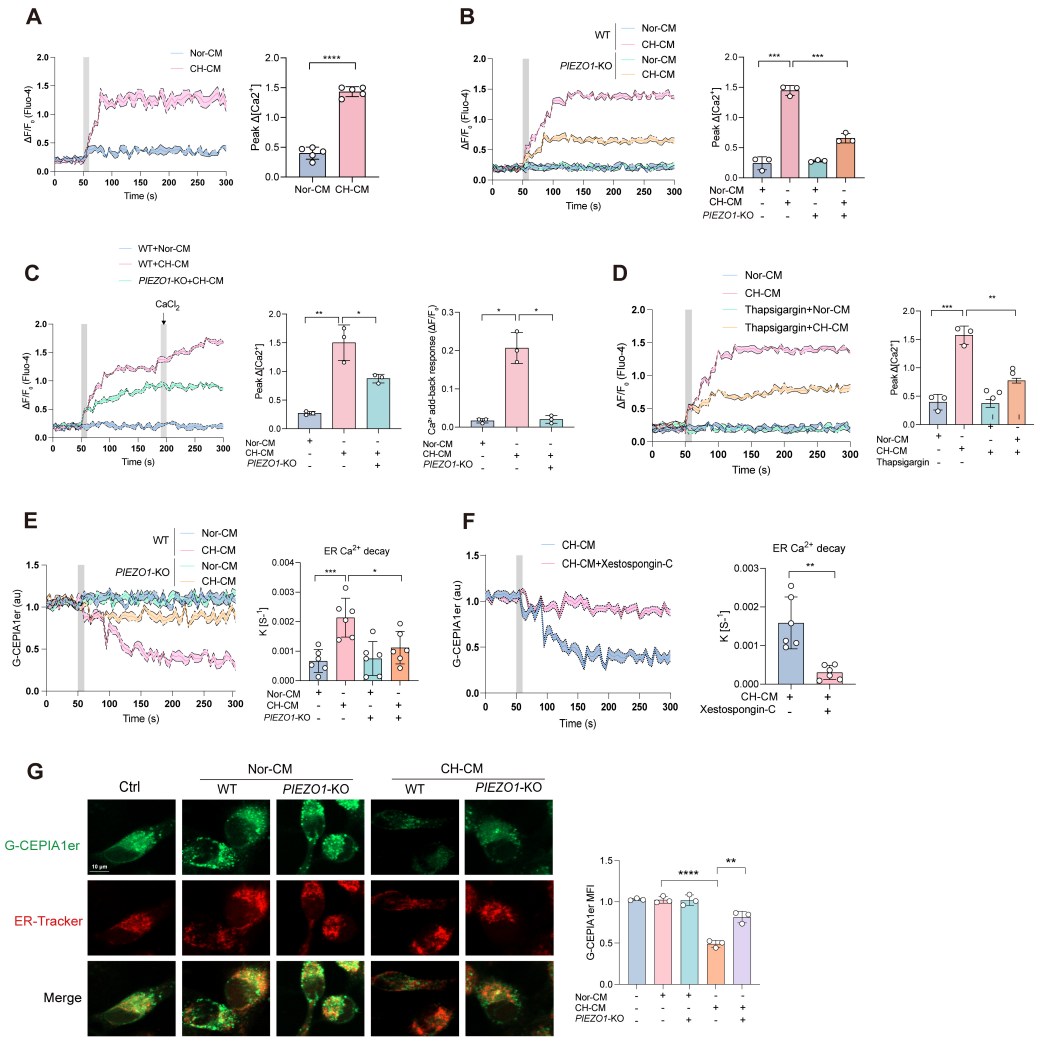

A
B
C
D
E
F
G
Nor-CM
CH-CM
WT
PIEZO1-KO
Time (s)
Peak Δ[Ca2+]
ΔF/F0 (Fluo-4)
CaCl2
WT+Nor-CM
WT+CH-CM
PIEZO1-KO+CH-CM
Ca2+ add-back response (ΔF/F0)
Thapsigargin+Nor-CM
Thapsigargin+CH-CM
Thapsigargin
G-CEPIA1er (au)
ER Ca2+ decay
K [S-1]
CH-CM+Xestospongin-C
Xestospongin-C
Ctrl
Nor-CM
CH-CM
G-CEPIA1er
ER-Tracker
Merge
G-CEPIA1er MFI

Figure 6. CH-CM elicits a PIEZO1-dependent Ca^{2+} response with ER-store mobilization.

(A) Real-time Fluo-4 AM fluorescence traces and peak-response quantification in BEAS-2B cells stimulated with Nor-CM or CH-CM (n = 5 independent experiments). **(B)** Real-time Fluo-4 AM fluorescence traces and peak-response quantification in WT and *PIEZO1*-KO cells exposed to Nor-CM or CH-CM (n = 4). **(C)** Cytosolic Ca^{2+} responses in nominally Ca^{2+}-free buffer followed by $CaCl_2$ add-back in WT cells treated with Nor-CM or CH-CM and in *PIEZO1*-KO cells treated with CH-CM (n = 3). The gray bar indicates CM addition, and the arrow indicates $CaCl_2$ add-back. Initial peak responses and Ca^{2+} add-back responses were quantified separately. **(D)** Real-time Fluo-4 AM fluorescence traces and peak-response quantification following ER-store depletion with thapsigargin (1 μM) before Nor-CM or CH-CM stimulation (n = 4). **(E)** Real-time G-CEPIA1er fluorescence and ER Ca^{2+} decay constants in WT and *PIEZO1*-KO cells exposed to Nor-CM or CH-CM (n = 6). **(F)** G-CEPIA1er responses to CH-CM with or without the IP3R inhibitor Xestospongin-C (n = 6). **(G)** Representative G-CEPIA1er/ER-Tracker images and G-CEPIA1er mean fluorescence intensity in untreated control, WT, and *PIEZO1*-KO cells exposed to Nor-CM or CH-CM (n = 3). Scale bar, 10 μm. Gray bars indicate stimulus addition. Data are presented as mean ± SD and were analyzed using two-tailed unpaired Student's *t*-tests or one- or two-way ANOVA followed by appropriate multiple-comparisons tests. *$P < 0.05$, ** $P < 0.01$, *** $P < 0.001$, **** $P < 0.0001$.

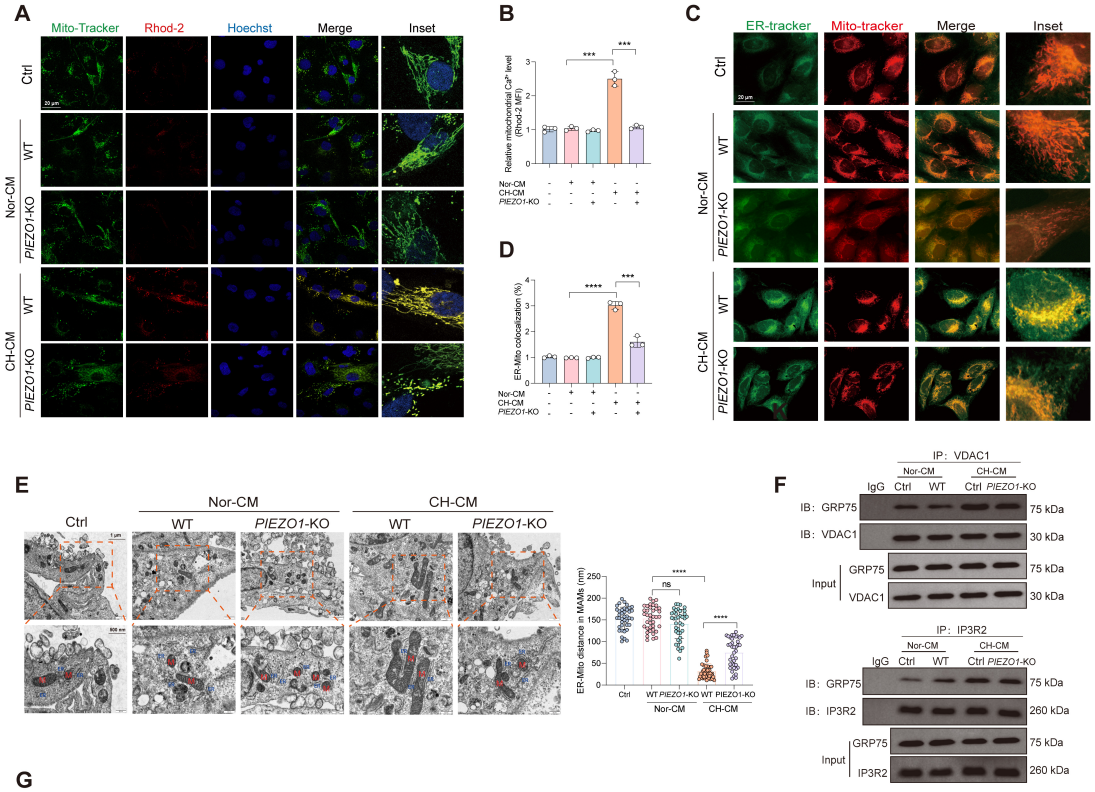

A
Mito-Tracker
Rhod-2
Hoechst
Merge
Inset
Ctrl
Nor-CM
CH-CM
WT
PIEZO1-KO
B
Relative mitochondrial Ca2+ level (Rhod-2 MFI)
C
ER-tracker
Mito-tracker
Merge
Inset
D
ER-Mito colocalization (%)
E
Ctrl
Nor-CM
CH-CM
WT
PIEZO1-KO
ER-Mito distance in MAMs (nm)
ns
F
IP: VDAC1
IgG
Ctrl
WT
Ctrl
PIEZO1-KO
IB: GRP75
IB: VDAC1
Input
75 kDa
30 kDa
IP: IP3R2
IB: IP3R2
260 kDa
G
IP3R2
GRP75
DAPI
Merge
VDAC1
IP3R2-GRP75 colocalization (%)
GRP75-VDAC1 colocalization (%)
H
kDa
GRP75
β-actin
75
42
Relative protein expression (GRP75/β-actin)
I
si-NC
si-GRP75
Yoda1
si-GRP75+Yoda1
Rhod2-AM MFI
J
PBS
Ru360
Yoda1
Ru360+Yoda1

Figure 7. PIEZO1 signaling promotes MAM remodeling and ER-to-mitochondrial Ca^{2+} transfer.

(A, B) Representative confocal images **(A)** and quantification **(B)** of mitochondrial-associated Rhod-2 fluorescence in WT and *PIEZO1*-KO BEAS-2B cells exposed to Nor-CM or CH-CM (n = 3 independent experiments). Mitochondria were labeled with MitoTracker Green and nuclei with Hoechst. **(C, D)** ER-Tracker/MitoTracker imaging and quantitative ER–mitochondrial colocalization analysis using Pearson's correlation coefficients and Manders overlap coefficients (M1/M2) (n = 3). **(E)** Representative TEM images of ER–mitochondrial contacts and quantification of inter-organelle distance (n = 3 independent experiments; multiple contacts were averaged within each experiment). Magnification: 5000/10000 ×, 80 kV. **(F)** Co-immunoprecipitation of GRP75 with VDAC1 or IP3R2 in WT and *PIEZO1*-KO cells exposed to Nor-CM or CH-CM. **(G)** Representative double-immunofluorescence images and quantitative colocalization analysis of IP3R2/GRP75 and GRP75/VDAC1 using Pearson's correlation coefficients and Manders overlap coefficients (M1/M2) (n = 3). **(H)** GRP75 Western blotting and quantification in WT and *PIEZO1*-KO cells exposed to Nor-CM or CH-CM (n = 3). **(I)** Rhod-2 flow-cytometric analysis after GRP75 knockdown with or without Yoda1 under CH-CM conditions (n = 4). **(J)** Rhod-2 analysis after MCU inhibition with Ru360 with or without Yoda1 (n = 5). β-actin served as the loading control. Scale bars are indicated in the images. Data are mean ± SD and were analyzed using one- or two-way ANOVA followed by appropriate multiple-comparisons tests. *$P < 0.05$, ** $P < 0.01$, *** $P < 0.001$, **** $P < 0.0001$; ns, not significant.

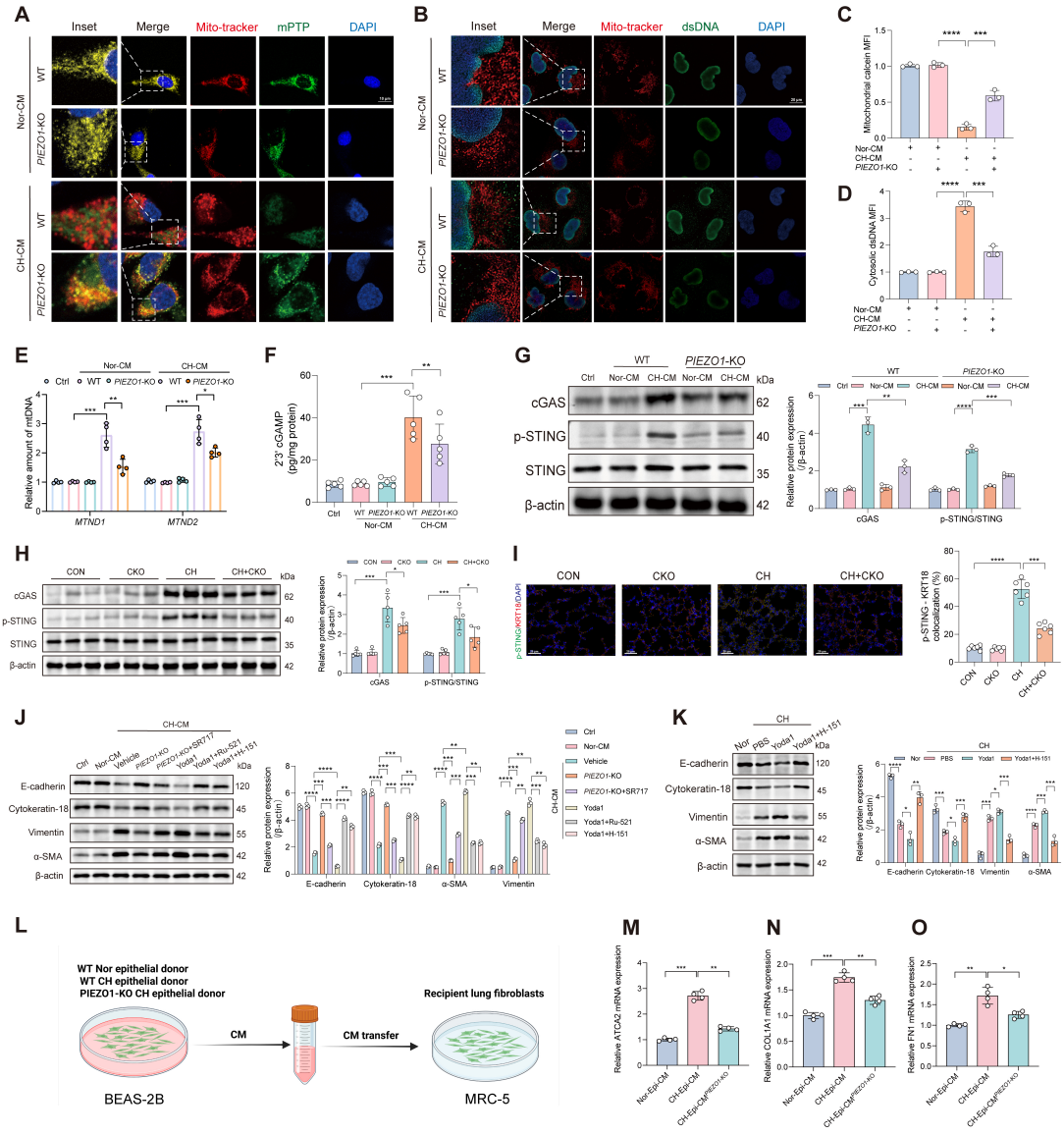

A
Inset
Merge
Mito-tracker
mPTP
DAPI
Nor-CM
CH-CM
WT
PIEZO1-KO
B
Inset
Merge
Mito-tracker
dsDNA
DAPI
C
Mitochondrial calcein MFI
D
Cytosolic dsDNA MFI
E
Relative amount of mtDNA
MTND1
MTND2
F
2'3' cGAMP (pg/mg protein)
G
cGAS
p-STING
STING
β-actin
Relative protein expression (/β-actin)
H
CON
CKO
CH
CH+CKO
I
p-STING-KRT18 colocalization (%)
J
CH-CM
E-cadherin
Cytokeratin-18
Vimentin
α-SMA
K
L
WT Nor epithelial donor
WT CH epithelial donor
PIEZO1-KO CH epithelial donor
CM
CM transfer
Recipient lung fibroblasts
BEAS-2B
MRC-5
M
Relative ATOA2 mRNA expression
N
Relative COL1A1 mRNA expression
O
Relative FN1 mRNA expression

Figure 8. PIEZO1-dependent mitochondrial injury promotes epithelial cGAS–STING activation and fibroblast activation-associated signaling.

(A) Representative calcein-AM/$CoCl_2$ assay of mPTP opening in WT and *PIEZO1*-KO BEAS-2B cells exposed to Nor-CM or CH-CM. Reduced mitochondrial calcein fluorescence indicates increased mPTP opening. **(B)** Representative confocal images of dsDNA and MitoTracker under the same conditions. Dashed boxes highlight extra-nuclear, extra-mitochondrial dsDNA signals. **(C)** Quantification of mitochondrial calcein fluorescence (n = 3 independent experiments). **(D)** Quantification of cytosolic dsDNA fluorescence (n = 3 independent experiments). **(E)** RT-qPCR quantification of cytosolic mtDNA (*MT-ND1* and *MT-ND2*) (n = 4 independent experiments). **(F)** Intracellular 2′3′-cGAMP concentrations (n = 5 independent experiments). **(G)** Western blotting and quantification of cGAS and p-STING/STING in WT and *PIEZO1*-KO cells exposed to Nor-CM or CH-CM (n = 3 independent experiments). **(H)** Western blotting and quantification of cGAS and p-STING/STING in lung homogenates from CON, CKO, CH, and CH+CKO mice (n = 5 mice/group). **(I)** Representative p-STING/KRT18 double-immunofluorescence and quantification of p-STING-positive signal within KRT18-positive epithelial regions (n = 6 mice/group). **(J)** Western blotting and quantification of EMT-associated proteins following *PIEZO1* deletion, STING activation with SR717, PIEZO1 activation with Yoda1, or inhibition with Ru.521 or H-151 under CH-CM conditions (n = 3 independent experiments). **(K)** Western blotting and quantification of EMT-associated proteins in Nor mice and CH mice treated with PBS, Yoda1, or Yoda1+H-151 (n = 3 mice/group). **(L)** Schematic of epithelial-to-fibroblast conditioned-medium transfer. **(M–O)** RT-qPCR analysis of *ACTA2* **(M)**, *COL1A1* **(N)**, and *FN1* **(O)** in MRC-5 fibroblasts treated with conditioned medium from Nor WT, CH WT, or CH *PIEZO1*-KO epithelial donor cells (n = 4 independently prepared CM batches). β-actin served as the loading control for Western blotting and as the reference gene for RT-qPCR normalization, as appropriate. Scale bars are indicated in the images. Data are mean ± SD and were analyzed using one- or two-way ANOVA followed by appropriate multiple-comparisons tests. *$P < 0.05$, ** $P < 0.01$, *** $P < 0.001$, **** $P < 0.0001$.